



Geochronology and geochemistry of the giant Qian'echong Mo deposit, Dabie Shan, eastern China: Implications for ore genesis and tectonic setting



Mei Mi^a, Yan-Jing Chen^{b,*}, Yong-Fei Yang^b, Pin Wang^a, Fa-Ling Li^c, Shou-Quan Wan^c, You-Ling Xu^c

^a Key Laboratory of Mineralogy and Metallogeny, Guangzhou Institute of Geochemistry, CAS, Guangzhou 510640, China

^b Key Laboratory of Orogen and Crust Evolution, Peking University, Beijing 100871, China

^c Geological Team 3, Henan Bureau of Land and Resources, Zhengzhou 464000, China

ARTICLE INFO

Article history:

Received 9 May 2014

Accepted 11 May 2014

Available online 4 June 2014

Handling Editor: R. Goldfarb

Keywords:

U–Pb geochronology

Re–Os geochronology

Sr–Nd–Pb isotopes

Qian'echong porphyry Mo deposit

Dabie Shan

ABSTRACT

The Qian'echong Mo deposit is a giant porphyry deposit in the Dabie Shan of eastern China. Molybdenum (Mo) mineralization mainly occurs as numerous veinlets in altered schists, with the development of potassic, phyllic, argillic, and propylitic alteration assemblages. A buried granite porphyry stock and locally exposed dikes are spatially and genetically related to the Mo mineralization. Zircon crystals from exposed quartz porphyry, rhyolitic porphyry, and granite porphyry dikes, as well as a buried granite porphyry dike yield weighted average $^{206}\text{Pb}/^{238}\text{U}$ ages of 128.9 ± 1.1 Ma (MSWD = 0.30, 2σ , $n = 13$), 127.42 ± 0.94 Ma (MSWD = 0.58, 2σ , $n = 17$), 127.44 ± 0.98 Ma (MSWD = 1.6, 2σ , $n = 16$), and 126.6 ± 1.4 Ma (MSWD = 0.67, 2σ , $n = 15$), respectively. The buried granite porphyry stock yields a zircon U–Pb weighted average age of 124.7 ± 1.6 Ma (MSWD = 1.5, 2σ , $n = 16$), which is slightly younger than the exposed dikes, but within error of the age of the buried granite porphyry dike. Five molybdenite samples from the ores yield Re–Os isotope ages of 123.31 ± 1.02 to 128.49 ± 1.40 Ma, which are consistent with the U–Pb ages for the igneous rocks. These age data constrain magmatic–hydrothermal activity at the Qian'echong Mo deposit to a period of about six million years from 129 to 123 Ma. This period overlaps the recognized regional Mo mineralization event in the Dabie Shan of 142–111 Ma, which took place during the post-collisional tectonism subsequent to amalgamation of the Yangtze and North China blocks.

The Qian'echong granite porphyry stock and dikes have high contents of SiO_2 , K_2O and Al_2O_3 , and low contents of TiO_2 , MgO and CaO , showing a peraluminous high-K calc-alkaline to shoshonite affinity, with obvious LREE enrichment and a negative Eu anomaly. The rocks have a high initial $^{87}\text{Sr}/^{86}\text{Sr}$ of 0.70729 to 0.71788 and highly negative $\epsilon_{\text{Nd}}(t)$ values of -16.2 to -26.1 , with $T_{\text{DM}2}(\text{Nd})$ ages of 2.24 to 3.03 Ga. Their $(^{206}\text{Pb}/^{204}\text{Pb})_t$, $(^{207}\text{Pb}/^{204}\text{Pb})_t$, and $(^{208}\text{Pb}/^{204}\text{Pb})_t$ values range from 16.017 to 16.701, 15.252 to 15.368, and 37.095 to 37.578, respectively. This Sr–Nd–Pb isotopic signature indicates that the causative granitic intrusions for the Qian'echong deposit were mainly melts with components of both the northern Dabie complex and the Taihua and Xiong'er Groups that are part of the Precambrian basement of the North China block. The melts were generated during the tectonic extrusion of the Dabie Shan and their emplacement onto the basement of the North China block. The Qian'echong Mo deposit is unique based upon the crustal source for the causative porphyry, localization of most mineralization in the surrounding schist country rocks, and the CO_2 -rich ore-forming fluid. Thus we propose the Qian'echong deposit to represent a new sub-type of porphyry Mo deposit, herein termed collisional- or Dabie-type porphyry deposit.

© 2014 International Association for Gondwana Research. Published by Elsevier B.V. All rights reserved.

1. Introduction

The majority of porphyry deposits are formed in magmatic arcs (Sillitoe, 1972; Richards, 2011), although a small number are considered to develop in other settings (e.g. Richards et al., 1990; Chen et al., 2000; Richards, 2003; Chen et al., 2007; Chen and Li, 2009; Pirajno, 2009; Richards, 2009; Pirajno, 2013). The east–west trending Qinling–Dabie

Shan, eastern China, is a Mesozoic collisional orogenic belt that sutures the Yangtze and the North China blocks, and accommodates one of the world's most important molybdenum (Mo) belts in the eastern Qinling area. The eastern Qinling part of the orogen contains six giant Mo deposits (each with a reserve of >0.5 Mt Mo) and tens of small (<0.01 Mt Mo), medium (0.01–0.1 Mt Mo), and large (0.1–0.5 Mt Mo) deposits, with a combined total reserve of ~ 6 Mt Mo metal (Li et al., 2007; Chen et al., 2009). These Mo deposits are mainly associated with Mesozoic porphyritic intrusions and are classified as porphyry or porphyry–skarn deposit types formed in a post-collisional regime (Chen

* Corresponding author.

E-mail addresses: yjchen@pku.edu.cn, gigyjchen@126.com (Y.-J. Chen).

et al., 2000; Li et al., 2007; Mao et al., 2008; Chen et al., 2009; Mao et al., 2010, 2011; N. Li et al., 2012a, 2012b; Chen, 2013; N. Li et al., 2013).

The Dabie Shan is the easternmost part of the Qinling–Dabie Shan orogenic belt. It has been regarded as a relatively nonprospective part of the orogen for a long time, because no important deposits had been discovered there (Chen and Wang, 2011). In the past decade, this changed with the discoveries of large to giant porphyry Mo deposits at Tangjiaping in 2004, Qian'echong in 2007, and Shapinggou in 2008, and small to medium Mo deposits at Zhupeidian, Liangshan, Yaochong, Dayinjian, Xiaofan, and Mushan (Fig. 1; Chen and Wang, 2011; Mao et al., 2011; Y.F. Yang et al., 2013; Y. Li et al., 2013; Gao et al., 2014; Wang et al., 2014). These deposits have shown the Dabie Shan to be a significant porphyry Mo belt, similar to the eastern Qinling, with proven reserves of >3 Mt Mo metal (Fig. 1; H.C. Li et al., 2012; N. Li et al., 2012).

The Qian'echong porphyry Mo deposit is the second largest Mo deposit in the Dabie Shan, and contains a proven reserve of about 741 Mt of ore at an average grade of 0.081% Mo (Geological Survey Team 3 of Henan Bureau of Land and Resources, 2009; Y.F. Yang et al., 2013). Although it is not being mined due to present economic conditions, the study of the geology, geochemistry and genesis of this large deposit remains important. M.Z. Yang et al. (2010) determined a U–Pb age of 128.8 ± 2.6 Ma for a weakly mineralized biotite granite porphyry dike at the deposit and a weighted average Re–Os age of 127.82 ± 0.87 Ma for molybdenite samples from the Qian'echong mineralization. Two other biotite granite porphyry dike samples yielded initial $^{87}\text{Sr}/^{86}\text{Sr}$ ratios of 0.70669 and 0.72165, and $\epsilon\text{Nd}(t)$ of -18.01 and -21.37 (M.Z. Yang et al., 2010), respectively. Gao et al. (2014) recently reported a

molybdenite Re–Os isochron age of 129.4 ± 1.5 Ma, and two SHRIMP zircon U–Pb ages of 130 ± 2 Ma and 129 ± 2 Ma, together with Pb–Sr–Nd isotope data for the buried granite porphyry.

Despite the above preliminary geochronological and geochemical work, a thorough and systematic study of the ages and Sr–Nd–Pb isotopic compositions of the buried main biotite granite porphyry stock and other porphyry dikes, such as the rhyolitic porphyry and quartz porphyry dikes, in this deposit is lacking. Consequently, the origin of the porphyry Mo system has not been well constrained. Therefore, we report here new zircon U–Pb isotope dates for all the ore-associated intrusions, additional molybdenite Re–Os dates of the ores, and major and trace element and Sr–Nd–Pb isotope data for the ore-associated intrusions to comprehensively define the duration of the magmatic–hydrothermal activity and place it into a well-constrained tectonic setting. Our results show that the Qian'echong porphyry Mo system originated from the southward subduction of the North China block, rather than by the previously-suggested northward subduction of the Yangtze block.

2. Regional geology

The Dabie Shan lies at the eastern end of the east–west-trending Qinling–Dabie Shan orogenic belt suturing the North China and Yangtze blocks (Zheng et al., 2013). It is bounded by the Xiangfan–Guangji fault to the south and the Luanchuan or inferred Gushi fault to the north (Fig. 1). The NW-trending Guishan–Meishan fault defines the final suturing between the North China and Yangtze blocks. To the north of Guishan–Meishan fault, metamorphic rocks of the Qinling and

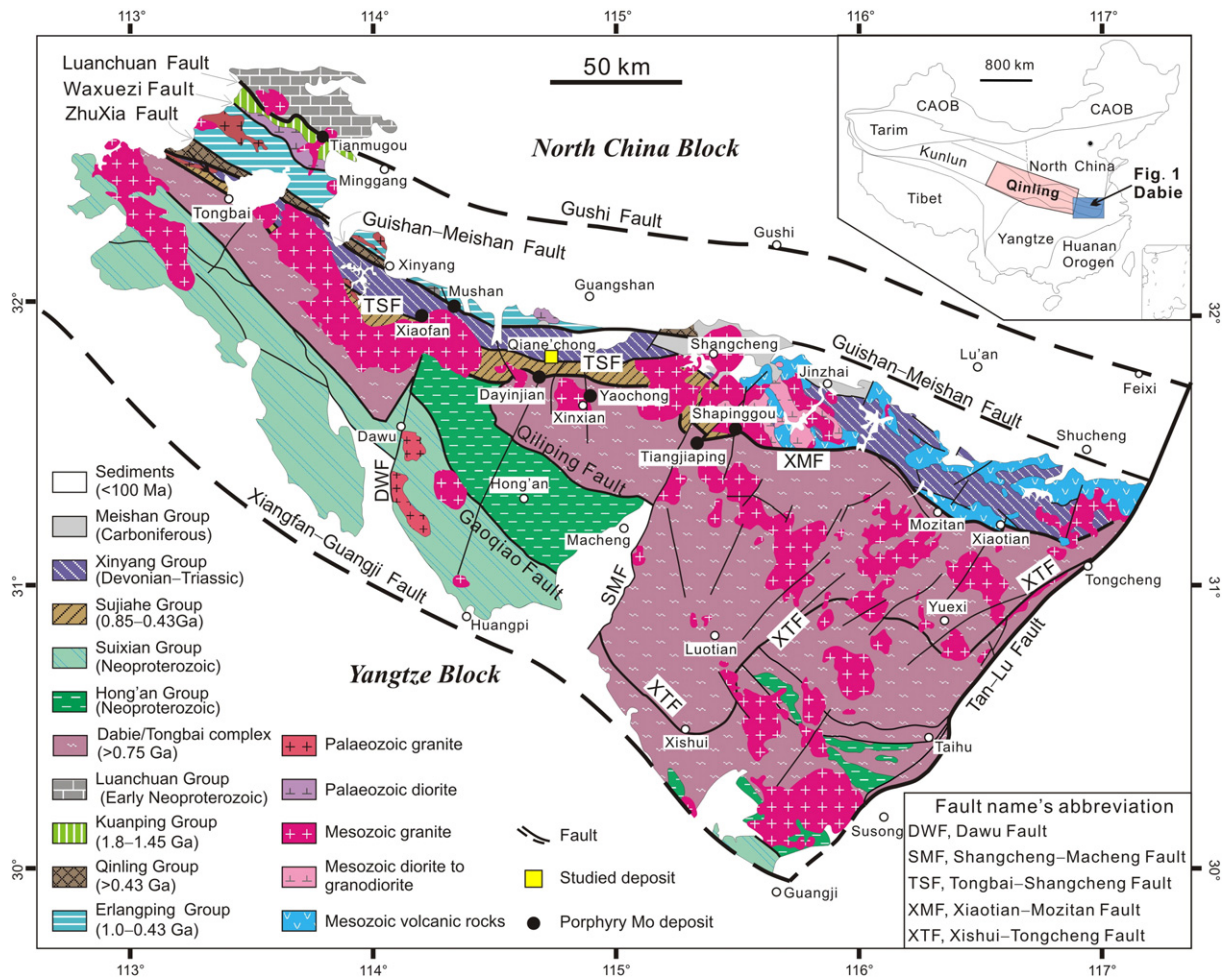


Fig. 1. Generalized geological map of the Dabie Shan, showing the locations of Qian'echong and other porphyry Mo deposits (modified after Chen and Wang, 2011). CAOB: Central Asian Orogenic Belt; COB: Central Orogenic Belt.

Erlangning Groups make up the Caledonian (early Paleozoic) accretionary belt formed along the southern margin of the North China block (Chen and Fu, 1992; Liu et al., 2013). They are locally overlain by late Paleozoic strata, such as the Carboniferous Meishan Group coal-bearing sequence. Progressively to the south of the Guishan–Meishan fault, are the rocks of the Xinyang Group, the Sujiahe Group (locally called Xiaojiamiao Formation at the Qian'echong deposit), the Dabie Complex, the Hong'an Group and the Suixian Group, with the Tongbai–Shangcheng (TSF), Xiaotian–Mozitan (XMF), Qiliping, and Gaoqiao faults as their boundaries, respectively (Fig. 1).

The Xinyang Group is a Hercynian–Indosinian (Devonian to Early Triassic) accretionary complex, containing ophiolitic slices and Precambrian fragments (Liu et al., 2013). It is subdivided into the Guishan and Nanwan Formations in ascending order, with lithologies being dominated by mafic to felsic volcanic and sedimentary rocks, respectively (Henan Bureau of Geology and Mineral Resources, 1989). The Guishan Formation, intercalated with ophiolitic slices of volcanic rocks from the Qinling Group, is dominated by fore-arc clastic sediments with minor marble. The Nanwan Formation is a greenschist facies assemblage of bedded quartzites and pelites (Liu et al., 2013).

The Sujiahe Group, constituting a Caledonian accretionary complex, comprises highly strained granites, metagabbro bodies, mica schists, quartzofeldspathic gneisses, amphibolites, marbles, and eclogite enclaves (X.C. Liu et al., 2008). The Dabie (or Tongbai) Complex, accommodating UHP eclogite massifs, consists of high-grade metamorphosed Neoproterozoic tonalite–trondhjemite–granodiorite (TTG) gneisses and subordinate migmatites (Jahn et al., 1999; Hacker et al., 2000; Zheng et al., 2006), and Archean to Proterozoic supracrustal rocks including granulites, amphibolites, biotite–plagioclase gneisses, and marbles (Liu and Liou, 2011). It is often subdivided into southern and northern Dabie complexes according to the protolith of the rocks, with the Xishui–Tongcheng fault (XTF; Fig. 1) as the boundary (Zhang et al., 2002; Zhao et al., 2008, 2011). The Hong'an Group (Neoproterozoic) comprises quartzofeldspathic schists, and muscovite–albite and two-mica gneisses, with minor eclogites, amphibolites, marbles, metaphosphorite layers, and graphite schist (Liu et al., 2004; X.C. Liu et al., 2008). The Suixian Group is a low to middle metamorphic grade Neoproterozoic volcanic–sedimentary sequence, containing voluminous blueschists, and thus is also called the Mulanshan blueschist unit (Liu et al., 2004; X.C. Liu et al., 2008).

Intrusions in Dabie Shan are mainly Jinningian (1.0–0.54 Ga) and Yanshanian (late Mesozoic) in age (Fig. 1). The Jinningian granitoids were emplaced into rocks of the Dabie Complex. Regional faults and tectonostratigraphic units in the Dabie Shan strike WNW to NW. They are crosscut by NE- to NNE-trending faults that developed in the Jurassic or later, such as the Dawu and Shangcheng–Macheng faults, and which typically control the location of the Yanshanian granitic batholiths and stocks. Yanshanian stocks, including Xiaofan, Mushan, Dayinjian, Tangjiaping, and Shapinggou, have zircon U–Pb ages of 142–110 Ma (H. Zhang et al., 2011; Mao et al., 2011; H.C. Li et al., 2012; Meng et al., 2012; H.J. Chen et al., 2013), and are associated with porphyry Mo deposits (Fig. 1; Y. Li et al., 2013 and references therein).

3. Local and ore geology

The Qian'echong Mo deposit is located in the northern Dabie Shan, to the south of the Guishan–Meishan fault (Fig. 1). Rocks of the Nanwan Formation of the Xinyang Group and of the Xiaojiamiao Formation crop out at the deposit, with the Tongbai–Shangcheng fault separating the two formations (Fig. 2). The Neoproterozoic–Ordovician Xiaojiamiao Formation consists of muscovite–albite schists, muscovite–quartz schists, two-mica oligoclase schists, and lenticular marble intercalations, whereas the Devonian–Triassic Nanwan Formation is composed of two-mica quartz schists, epidote–biotite quartz schists, and biotite–plagioclase schists.

Structures in the deposit area are dominated by two groups of faults subsidiary to the regional Tongbai–Shangcheng fault. The WNW- to NW-trending faults are the most conspicuous, and are as long as 600–2500 m, with widths of 0.5–5 m, and SW-dips with angles of 70–90°. The NNE- to NNW-trending faults are hundreds to thousands of meters in length, with widths of 0.5–10 m, and steep dips to either the west or the east at angles of 70–90°. They locally crosscut the WNW- to NW-trending faults (Fig. 2).

Three types of igneous dikes crop out in the Qian'echong area (Fig. 2). Diorite dike swarms are WNW-trending, and composed of plagioclase, hornblende, K-feldspar, and quartz, with accessory apatite and magnetite. These dikes are crosscut by NNE- to NNW-trending faults and quartz porphyry dikes, which comprise quartz, K-feldspar, plagioclase, and minor mica. Rhyolitic to granite porphyry dikes occur along the WNW-trending faults and are composed of quartz, plagioclase, K-feldspar, and minor biotite phenocrysts. The rhyolitic porphyry dikes have similar mineralogy to granite porphyry dikes, but the phenocrysts are more idiomorphic and the grains of the matrix are too fine to be visible. No crosscutting relationship has been observed between the rhyolitic to granitic porphyry dikes and the diorite or the quartz porphyry dikes.

The ore-associated Qian'echong granite porphyry stock intruded schists of the Nanwan Formation and is totally under cover (Fig. 3). It was discovered by 10 drill holes between the seventh and eighth prospecting lines at depths of –607 to –745 m ASL. As revealed by the drill hole data, the stock is ~500-m-long, ~400-m-wide, and elongated in a WNW direction. It may connect upward to the thin granite

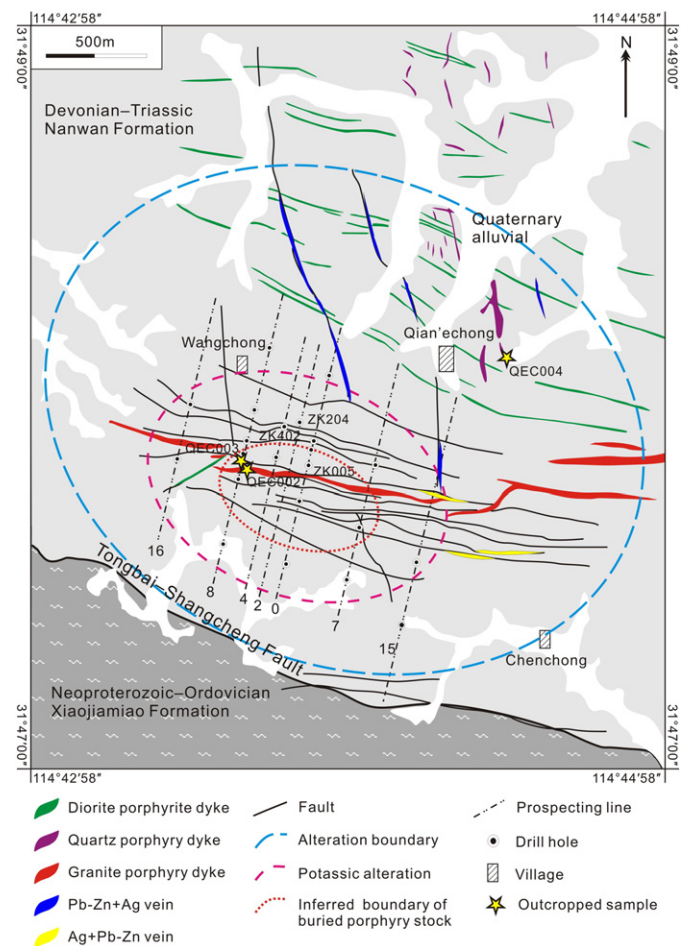


Fig. 2. Simplified geological map of the Qian'echong Mo deposit. Modified after Geological Survey Team 3 of Henan Bureau of Land and Resources (2009).

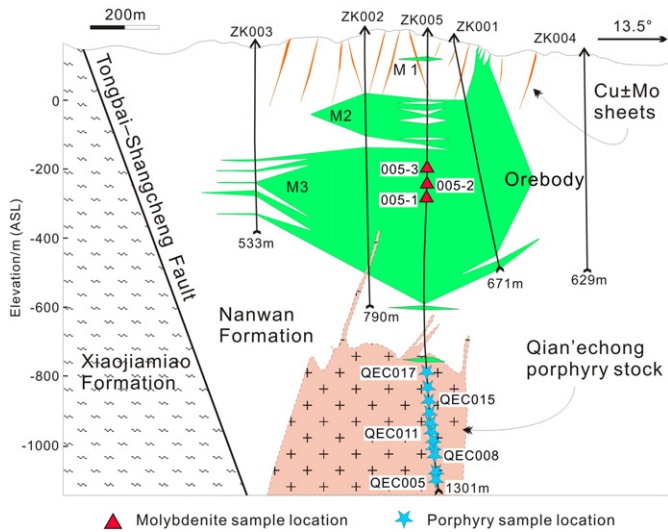


Fig. 3. Generalized geological cross-section along prospecting line no. 0 of the Qian'echong deposit, showing the occurrence of the main orebodies and relationship to underlying granite porphyry.

Modified after Geological Survey Team 3 of Henan Bureau of Land and Resources (2009).

porphyry dikes, also recognized in the drill holes, and then to the granitic to rhyolitic dikes observed at surface. The granite porphyry stock contains 30–40% phenocrysts of plagioclase, K-feldspar, quartz, and minor biotite. The matrix comprises fine-grained K-feldspar, plagioclase, quartz, and biotite, with minor sphene, zircon, apatite, magnetite, and ilmenite.

Field observations reveal that the quartz porphyry dikes and the rhyolitic to granite porphyry dikes host minor Mo mineralization, although they are significantly above the main orebodies. Drill hole data indicate that the buried granite porphyry dikes and stock are mineralized and hydrothermally altered, but also do not contain much of the ore (<1% of the calculated reserve). However, the magmatic rocks are surrounded by a broad hydrothermal alteration system in the country rock schists, consisting of a potassic alteration core, a huge concentric propylitic alteration halo, and an intermediate zone of phyllic alteration that also strongly overprinted the potassic zone. The potassic core, marked by strong K-feldspar development, surrounds the stock in an elliptic form and with a diameter of 1–1.5 km (Fig. 2). The hydrothermal altered rocks host metallic mineralization that exhibits outward/upward zoning from Mo, through Cu–Mo, and to Pb–Zn–Ag (Figs. 2 and 3).

The Pb–Zn–Ag mineralization is present as sulfide-quartz ± calcite veins in the propylitically altered schist (Fig. 2) along the WNW- and NNW-trending faults. The largest vein is 800-m-long, 115- to 237-m-deep, and 1.8- to 6.7-m-wide, and NNW-trending with a dip of 75–85°. Metallic minerals in these veins are sphalerite, galena, and pyrite, with traces of chalcopyrite, tetrahedrite, argentite, and native silver. The veins have average grades of ~1% Pb, ~1% Zn, ~50 g/t Ag, and <0.2% Cu, respectively. Those veins with grades of >60 g/t Ag are referred to as “Ag veins” by local geologists. The three largest Ag veins are 150- to 330-m-long, 0.7- to 1.1-m-wide, and grade 60–170 g/t Ag. They occur to the east of the sheeted Cu ± Mo veins (see below), are along the WNW-trending faults, and dip to the south at 70–80°.

Numerous sheeted chalcopyrite- and molybdenite-bearing quartz veins are observed at the surface or at shallow levels in the potassic alteration zone (Figs. 2, 3). The sheeted Cu ± Mo veins are generally 0.5- to 2.5-m-wide and 150- to 350-m-long, are located along WNW-trending faults, and dip to the south at 70–80°, although some also dip steeply to the north (Fig. 3). The Mo grades in the veins are lower than 0.03%, but the Cu contents range from 0.38–1.21% at depths of 15–70 m. The veins become shorter, thinner, and more stockwork-like with increasing depths, and transition into fine stockwork networks and disseminations in the main Mo orebodies at depth.

Three main Mo orebodies (M1, M2, and M3 in Fig. 3) are hosted in the potassically altered schists. They mainly occur at elevations between 10 m and –600 m ASL, and immediately below the zone of sheeted Cu ± Mo veins, but above the Qian'echong granite porphyry stock (Fig. 3). The largest of these orebodies is about 1500-m-long, 400- to 1000-m-wide, and lenticular in shape. Ore minerals are mainly molybdenite and pyrite, with minor magnetite, chalcopyrite, galena, and sphalerite. Gangue minerals include quartz, feldspar, epidote, biotite, sericite, chlorite, fluorite, and calcite. Mineralization occurs as veinlets and stockworks with thicknesses of several to tens of millimeters, and as disseminations with flaky, replacement, idiomorphic to hypidiomorphic grains (Y.F. Yang et al., 2013).

Hydrothermal alteration types at the Qian'echong deposit include (Y.F. Yang et al., 2013): (1) potassic alteration, with biotite and K-feldspar as predominant hydrothermal minerals, occurring in the granitic porphyry stock and in the surrounding schists and adjacent dikes; (2) common silicification, particularly associated with quartz-sulfide stockworks or veinlets; (3) sericitization of feldspar and biotite, in association with disseminated pyrite and quartz-sericite veinlets; (4) argillization, typified by transformation of feldspar to kaolinite, generally adjacent to Mo-bearing quartz stockworks, rhyolitic to granitic dikes, and fractures in the feldspathic schists; (5) propylitization, with epidote, chlorite, sericite, and calcite as the predominant hydrothermal minerals; (6) carbonatization, mainly typified by carbonate veinlets; and (7) fluoritization, characterized by disseminated purple fluorite grains or veinlets.

The hydrothermal alteration and mineralization are divided into four stages, according to mineralogical features, associations and cross-cutting relationships of veins, as well as the mineral replacing relationships and petrographic characteristics of the altered rocks. Stage 1 is characterized by the assemblage K-feldspar + quartz + epidote + magnetite + pyrite. Magnetite is mostly disseminated, coexisting with K-feldspar, quartz, and epidote; pyrite forms idiomorphic to hypidiomorphic cubes or replaces magnetite; and minor molybdenite is disseminated in the porphyry. The minerals are zoned outward from potassic assemblages, to a zone of silicification, and to an outermost propylitic assemblage. Stage 2 was responsible for most of the Mo mineralization, and is characterized by the assemblage quartz + molybdenite + pyrite. Molybdenite is flaky, and is present in quartz-molybdenite ± pyrite stockworks or as fine-grained films coating cracks. Stage 3 is characterized by the assemblage of quartz ± calcite + base metal sulfides. The sulfides, including sphalerite, galena, pyrite, and chalcopyrite, are generally xenomorphic and coexist with quartz and calcite in veins. Silicification and phyllic alteration are most conspicuous in Stages 2 and 3. Stage 4 is characterized by quartz-carbonate, carbonate, or/and carbonate-fluorite veinlets, with no or little sulfide, which crosscut the earlier veins, stockworks, and altered porphyry assemblages.

Y.F. Yang et al. (2013) conducted initial fluid inclusion studies on the ores. Carbonic, carbonic-aqueous, aqueous, and solid-bearing fluid inclusions are present in the Stage 1 quartz. The Stage 2 quartz also contains the latter three types of inclusions. The Stage 3 inclusions are aqueous, with or without daughter minerals, but lack any detectable CO₂. The Stage 4 minerals only contain aqueous inclusions without daughter phases. Thus the hydrothermal fluids evolved from high-salinity and CO₂-rich ore fluids, to low-salinity and CO₂-poor post-ore fluids. The fluid inclusions in minerals of Stages 1, 2, and 3 homogenized at temperatures of 260–400 °C, 200–340 °C and 160–300 °C, respectively. The estimated minimum trapping pressures are as much as 100 MPa in Stage 1 and 62 MPa in Stage 2, corresponding to an initial mineralization depth of at least ~4 km (Y.F. Yang et al., 2013). Considering the observed chalcopyrite, calcite, and sylvite, but the absence of halite in solid-bearing inclusions, Y.F. Yang et al. (2013) proposed that the Qian'echong hydrothermal system was NaCl-poor. This characteristic, together with the initial CO₂-rich nature of the fluids and the widespread potassic alteration and fluoritization, is consistent with the

features proposed by Chen and Li (2009) for magmatic–hydrothermal systems that evolved in continental collision settings.

4. Sampling and analytical methods

4.1. Samples

Samples QEC002, QEC003, and QEC004 were collected from partly weathered outcropping granite porphyry, rhyolite porphyry, and quartz porphyry dikes, respectively (Fig. 2). Ten samples of the buried granite porphyry stock (QEC005–QEC016) were collected from core in drill hole ZK005 between depths of 1285 and 995 m (Figs. 2 and 3); whereas three samples of buried biotite granite porphyry dike (QEC018–QEC020) were collected from core in hole ZK204 at a depth of about 100 m. Due to the potassic, phyllic, and argillic alteration of much of the studied drill cores, care was taken in selecting the least altered samples for major and trace element and whole-rock Sr–Nd–Pb isotopic analyses.

The samples of buried granite porphyry stock show massive structure (Fig. 4A). The phenocrysts are composed of K-feldspar, quartz, and plagioclase, accounting for about 20%, 10%, and 5% of the rock volume, respectively, with lengths as great as 10 mm, but typically about 1–5 mm (Fig. 4B). The matrix shows a granitic texture (Fig. 4C), and mainly consists of fine-grained K-feldspar, quartz, plagioclase, and biotite.

Three samples of buried granite porphyry dike are more porphyritic (Fig. 4D) than the granite porphyry stock. The quartz phenocrysts account for about 20% of the rock volume, with maximum lengths of approximately 1 to 3 mm (Fig. 4E); the K-feldspar phenocrysts are present as tabular crystals, 1–3.5 mm in length, and account for about 20% of the rock volume (Fig. 4F); and the plagioclase and minor biotite phenocrysts together account for about 10% of the volume. The K-feldspar and plagioclase phenocrysts have undergone either sericitization or argillitization (Fig. 4F). The matrix, accounting for about 50% of the rock volume, is comprised of fine-grained K-feldspar, plagioclase, quartz, and biotite.

The samples from outcrops of rhyolitic to granitic porphyry dikes are obviously weathered and more porphyritic. They have micro-grained groundmasses (Fig. 4G, H) that are clearly less crystallized than the buried biotite granite porphyry dikes or stock. The phenocrysts account for about 45% of the volume, and mainly consist of quartz, followed by K-feldspar and biotite (Fig. 4G, H). The K-feldspar and biotite phenocrysts have been altered to sericite (Fig. 4H), whereas the quartz phenocrysts are typically broken or fractured. The grains of matrix are very fine, showing a microcrystalline to cryptocrystalline structure.

The quartz porphyry dike sample is also weathered. The phenocrysts are rounded xenomorphic quartz (Fig. 4I), and account for 10–25% of the rock volume, with maximum dimensions of about 0.5 to 1 mm. Potassium-feldspar phenocrysts can be observed locally. The matrix shows a microcrystalline to cryptocrystalline structure.

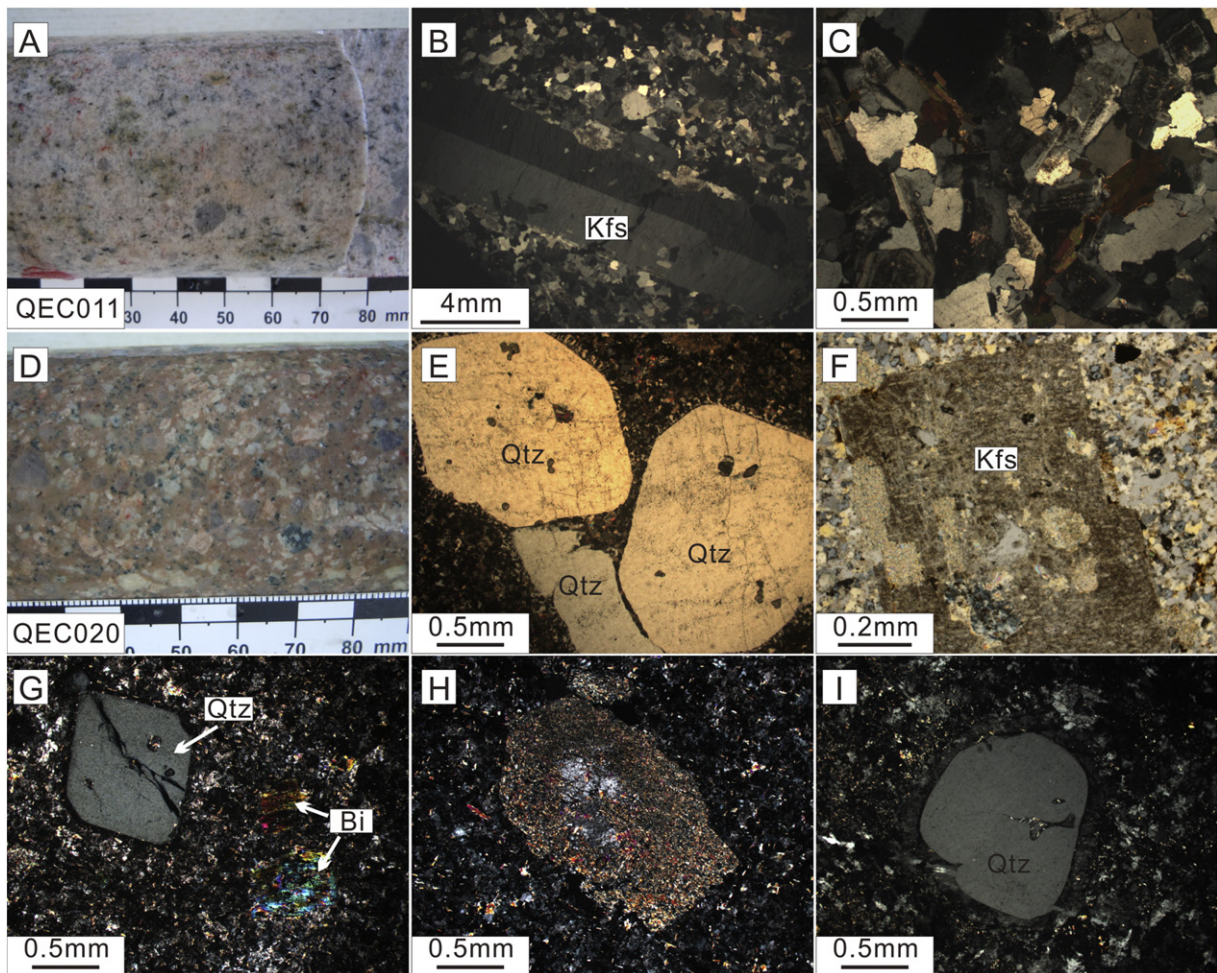


Fig. 4. Photographs showing petrography of the porphyry dikes and stock at Qian'echong. (A) Buried biotite granite porphyry stock; (B) K-feldspar phenocryst in the biotite granite porphyry (crossed nicols); (C) matrix of the biotite granite porphyry, showing granitic texture (crossed nicols); (D) biotite granite porphyry dike; (E) quartz phenocrysts in the biotite granite porphyry dike (crossed nicols); (F) K-feldspar phenocryst in the biotite granite porphyry dike; (G) quartz and biotite phenocrysts in the rhyolitic porphyry (crossed nicols); (H) sericitized K-feldspar phenocryst in the rhyolitic porphyry (crossed nicols); (I) the quartz phenocryst in the quartz porphyry dike (crossed nicols).

Table 1

Major and trace element compositions of the intrusions at Qian'echong deposit (wt.% for oxides, ppm for other elements).

No.	QEC 002	QEC 003	QEC 004	QEC 005	QEC 006	QEC 008	QEC 009	QEC 010	QEC 011	QEC 012	QEC 014	QEC 015	QEC 016	QEC 018	QEC 019	QEC 020
SiO ₂	77.21	76.46	76.76	72.76	72.88	73.35	73.04	72.86	72.57	72.38	73.14	72.39	72.54	72.50	72.58	72.65
TiO ₂	0.237	0.121	0.068	0.187	0.193	0.204	0.232	0.237	0.226	0.207	0.202	0.211	0.214	0.222	0.237	0.216
Al ₂ O ₃	12.60	13.56	12.27	14.82	14.64	14.40	14.22	14.28	14.25	14.59	14.16	14.36	14.24	14.01	14.09	13.89
CaO	0.06	0.07	0.04	1.19	0.95	1.14	1.02	1.03	1.21	1.08	0.91	1.09	0.94	1.30	1.24	1.36
TFe ₂ O ₃	1.15	0.55	0.95	1.12	1.11	1.34	1.51	1.60	1.52	1.22	1.06	1.09	1.03	1.46	1.46	1.39
Na ₂ O	0.01	2.09	0.07	3.88	3.77	3.75	3.84	3.70	3.77	3.80	3.64	3.77	3.83	3.61	3.63	3.41
K ₂ O	5.52	5.23	8.22	4.98	5.09	4.85	4.83	4.99	4.81	5.23	5.21	5.11	5.17	4.90	4.90	4.72
MgO	0.449	0.263	0.140	0.346	0.341	0.345	0.388	0.353	0.382	0.40	0.38	0.39	0.41	0.370	0.373	0.378
MnO	0.00	0.00	0.01	0.03	0.02	0.03	0.03	0.03	0.03	0.03	0.03	0.04	0.04	0.05	0.05	0.04
P ₂ O ₅	0.027	0.010	0.014	0.058	0.059	0.063	0.072	0.074	0.071	0.062	0.058	0.062	0.064	0.075	0.074	0.070
LOI	2.45	1.50	1.21	0.60	0.91	0.48	0.78	0.77	1.07	0.70	0.92	1.20	1.22	1.41	1.31	1.75
Total	99.73	99.88	99.77	99.98	99.97	99.96	99.96	99.94	99.92	99.70	99.71	99.72	99.71	99.90	99.94	99.88
Na ₂ O + K ₂ O	5.54	7.32	8.30	8.86	8.86	8.60	8.67	8.69	8.58	9.03	8.86	8.88	9.01	8.51	8.53	8.13
K ₂ O/Na ₂ O	454.2	2.5	111.7	1.3	1.4	1.3	1.3	1.3	1.3	1.4	1.4	1.4	1.3	1.4	1.3	1.4
A/CNK	2.06	1.47	1.35	1.06	1.09	1.07	1.06	1.07	1.05	1.05	1.07	1.05	1.05	1.03	1.04	1.05
A/NK	2.10	1.49	1.36	1.26	1.25	1.26	1.23	1.24	1.25	1.22	1.22	1.22	1.19	1.24	1.25	1.29
Mg#	43.7	48.5	22.6	37.9	37.8	33.9	33.8	30.4	33.2	39.3	41.2	41.3	44.2	33.4	33.7	35.0
Sc	1.72	2.24	1.64	1.26	1.37	1.61	1.60	1.69	1.73	1.34	1.17	1.29	1.19	1.69	1.88	1.81
V	16.62	7.65	6.70	14.39	14.21	15.87	15.95	15.28	16.96	18.14	14.71	16.16	14.58	18.65	15.84	18.02
Cr	4.70	3.32	2.79	6.50	6.37	7.52	7.12	3.83	6.64	9.20	6.43	5.72	6.28	8.47	6.97	6.97
Mn	30.8	17.3	93.1	226.7	215.5	239.0	266.9	234.8	296.0	228.5	231.5	280.3	283.2	448.6	449.3	318.6
Co	0.77	0.55	0.25	1.75	1.65	1.99	1.93	2.22	2.29	1.91	1.55	1.34	2.22	1.49	1.91	2.10
Ni	2.62	2.37	2.16	2.95	2.33	2.95	3.26	1.58	2.38	3.18	2.24	2.16	2.72	4.06	3.88	2.89
Cu	2.40	9.51	16.28	7.15	4.63	2.60	9.14	2.35	2.21	2.80	39.98	15.45	12.02	4.14	3.58	1.87
Zn	100.1	97.53	71.13	21.12	19.83	23.48	24.88	26.62	27.03	20.11	21.95	18.34	26.35	351.7	287.8	29.17
Ga	17.53	19.53	10.64	19.23	19.95	20.44	18.83	20.06	20.61	18.96	18.23	19.41	18.49	20.39	19.35	19.02
Ge	1.47	1.53	1.61	0.96	1.06	1.35	1.29	1.35	1.30	1.14	1.19	1.34	1.12	1.74	1.84	1.54
Rb	230.6	273.9	300.8	182.0	192.4	176.3	185.5	185.3	193.6	197.1	230.2	234.3	256.4	259.3	239.7	201.1
Sr	49.6	65.6	81.5	303.7	262.2	284.1	244.9	251.2	263.3	275.3	250.7	293.1	246.3	244.1	241.6	229.1
Zr	165.8	109.8	83.9	162.3	160.0	171.3	172.1	181.2	184.1	154.7	156.3	161.6	169.3	159.5	150.6	153.9
Nb	18.51	24.55	18.80	14.62	14.89	19.45	18.99	22.12	19.41	12.61	12.78	13.21	13.43	16.12	18.66	18.39
Cs	4.50	4.71	3.29	2.59	3.18	1.94	2.69	2.90	2.87	3.08	3.20	2.88	3.44	4.01	3.73	3.92
Ba	839	442	539	1372	1311	1106	962	928	1114	1327	1279	1314	1388	837	857	828
Hf	4.80	4.33	3.66	4.66	4.56	4.93	5.02	5.25	5.50	4.41	4.49	4.56	4.73	4.70	4.49	4.67
Ta	1.86	2.41	1.50	1.78	1.53	2.22	1.80	2.79	2.16	1.08	1.26	1.25	1.29	1.81	1.85	1.93
Pb	10.88	12.97	54.05	35.59	34.84	32.23	28.90	31.00	29.00	33.55	32.06	29.97	32.51	233.2	98.87	25.40
Th	28.78	28.45	13.20	23.06	24.68	22.23	26.33	23.41	23.63	24.28	23.38	23.20	25.95	27.26	25.48	29.13
U	2.36	6.63	2.70	4.98	7.42	8.18	6.12	7.60	6.97	3.15	4.39	4.51	4.79	8.33	7.80	8.33
Y	11.22	7.78	15.04	7.05	7.45	9.40	8.90	13.00	9.71	6.51	6.79	6.69	7.18	10.09	10.53	10.15
La	50.41	25.40	22.03	58.36	57.07	51.28	52.47	43.33	49.05	56.58	50.43	56.05	61.39	42.15	47.79	45.33
Ce	82.55	43.98	45.62	91.94	91.78	83.37	84.59	73.25	82.19	90.27	80.96	88.35	97.21	71.06	78.99	75.20
Pr	8.46	4.56	5.38	8.97	9.32	8.25	8.40	7.76	8.03	8.73	8.11	8.73	9.61	7.20	8.17	7.63
Nd	26.77	14.07	18.64	28.66	28.84	25.98	26.57	25.84	25.74	27.66	25.37	27.45	29.76	23.08	25.88	23.62
Sm	3.74	2.10	3.87	3.75	3.85	3.52	3.67	4.16	3.70	3.54	3.44	3.54	3.88	3.35	3.71	3.39
Eu	0.80	0.35	0.40	0.85	0.82	0.83	0.77	0.80	0.83	0.83	0.80	0.83	0.82	0.74	0.73	0.69
Gd	2.91	1.66	3.26	2.70	2.80	2.67	2.95	3.48	2.85	2.52	2.52	2.57	2.81	2.64	2.88	2.73
Tb	0.37	0.22	0.48	0.29	0.29	0.32	0.32	0.44	0.33	0.26	0.27	0.27	0.29	0.33	0.34	0.32
Dy	1.84	1.12	2.56	1.22	1.36	1.54	1.49	2.27	1.65	1.14	1.21	1.14	1.23	1.63	1.70	1.62
Ho	0.35	0.23	0.49	0.21	0.23	0.28	0.28	0.40	0.29	0.20	0.21	0.20	0.21	0.30	0.32	0.30
Er	0.90	0.64	1.24	0.54	0.58	0.73	0.70	0.99	0.75	0.50	0.51	0.50	0.53	0.79	0.84	0.80
Tm	0.14	0.12	0.19	0.08	0.08	0.12	0.11	0.16	0.12	0.07	0.08	0.07	0.08	0.13	0.13	0.13
Yb	0.97	0.91	1.29	0.52	0.53	0.80	0.72	1.05	0.84	0.49	0.49	0.50	0.53	0.90	0.92	0.91
Lu	0.16	0.16	0.20	0.08	0.08	0.13	0.12	0.16	0.13	0.08	0.08	0.08	0.08	0.15	0.14	0.15
REE + Y	191.59	103.29	120.68	205.20	205.06	189.21	192.06	177.08	186.18	199.37	181.24	196.97	215.62	164.53	183.07	172.97
δEu	0.72	0.56	0.33	0.77	0.73	0.80	0.69	0.62	0.75	0.81	0.80	0.80	0.72	0.73	0.66	0.68
(La/Yb) _N	37.24	20.09	12.25	81.28	77.97	45.81	52.42	29.71	42.04	82.83	73.97	79.77	82.77	33.59	37.30	35.69

QEC002, granite porphyry dike; QEC003, rhyolite porphyry dike; QEC004, quartz porphyry dike; QEC018–QEC020, biotite granite porphyry dike; QEC005, QEC006, QEC008–QEC012, QEC014–QEC016, biotite granite porphyry stock. A/CNK = Al₂O₃/(CaO + Na₂O + K₂O) in molecular ratio; A/NK = Al₂O₃/(Na₂O + K₂O) in molecular ratio; Mg# = 100 × Mg/(Mg + ΣFe) in atomic ratio.

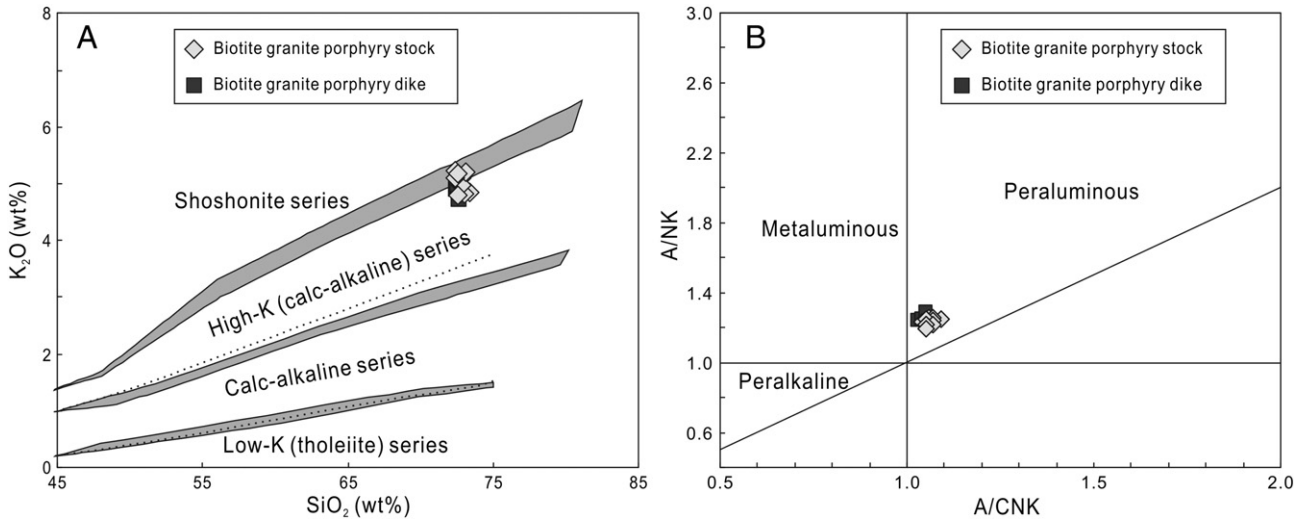


Fig. 5. Petrochemical discrimination diagrams of the buried granite porphyry stock and dikes at Qian'echong.

Five molybdenite samples for Re–Os isotopic dating were separated from the Stage 2 quartz–molybdenite veinlets, which were collected from ZK005 at depths of 300 to 430 m (Figs. 2 and 3) and ZK402 (Fig. 2) at depths of 118 to 300 m.

4.2. Analytical methods

Major and trace element analyses were performed at the Key Laboratory of Isotope Geochronology and Geochemistry, Guangzhou Institute of Geochemistry, Chinese Academy of Sciences (CAS), using XRF (X-Ray Fluorescence) on a Rigaku ZSX100e instrument and a Perkin-Elmer Sciex ELAN 6000 inductively coupled plasma mass spectrometer (ICP-MS), respectively. Details of the analytical procedures were given by Lee et al. (1997) and Li (1997). Accuracies of analyses are within 3% for major oxides and within 5% for trace elements.

Zircon grains were separated from samples QEC002, QEC003, QEC004, QEC011, and QEC020, using standard density and magnetic separation techniques. Representative zircon grains were mounted in epoxy resin and polished down to expose the grain center. Transmitted and reflected light micrographs and cathodoluminescence (CL) imaging were used to reveal internal structures of these zircon grains.

Measurements of U, Th, and Pb of zircons from samples QEC002, QEC003, QEC004, and QEC020 using a Cameca IMS 1280 large-radius SIMS at the Institute of Geology and Geophysics, CAS, Beijing. Analytical procedures are described by Li et al. (2009). The calibration of U–Th–Pb ratios was performed relative to standard zircon Plésovice (337 Ma, Sláma et al., 2008), and the correction of U concentrations was done by normalization to standard zircon 91500 (81 ppm; Wiedenbeck et al., 1995). A long-term uncertainty of 1.5% (1RSD) for ²⁰⁶Pb/²³⁸U measurements of the standard zircons was propagated to the unknowns (Li et al., 2010), despite the fact that the measured ²⁰⁶Pb/²³⁸U error in a specific session is generally ≤ 1%. Standard zircon Qinghu (159.5 Ma; Li et al., 2009) was alternately analyzed as an unknown sample to monitor the external uncertainties of SIMS U–Pb measurements calibrated against standard 91500. Measured compositions were corrected for common Pb using non-radiogenic ²⁰⁴Pb. Corrections are sufficiently small to be insensitive to the choice of common Pb composition, and an average of present-day crustal composition (Stacey and Kramers, 1975) is used for the common Pb assuming that the common Pb is mainly surface contamination introduced during sample preparation. Uncertainties for individual analyses in data tables are reported at a 1σ level; mean ages for pooled U/Pb analyses are quoted at a 2σ level. Data reduction was carried out using the Isoplot/Ex v.3.0 program (Ludwig, 2003).

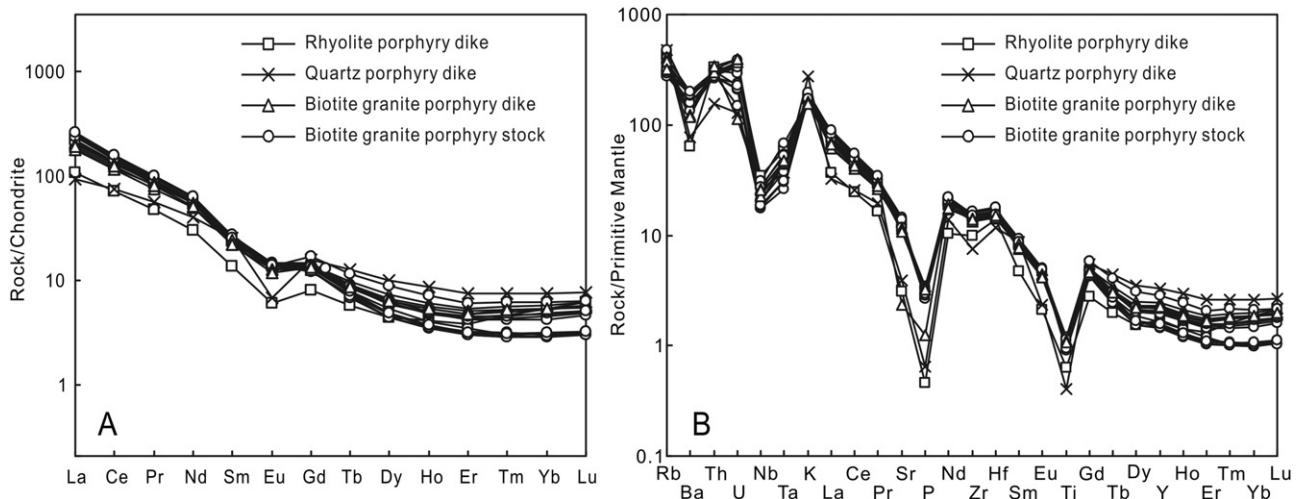


Fig. 6. Chondrite-normalized REE patterns (A) and primitive mantle-normalized trace element patterns (B) of the porphyries at Qian'echong deposit. Data of chondrite and primitive mantle are given by Sun and McDonough (1989).

Measurements of U, Th, and Pb concentrations of zircons from the sample QEC011 (the biotite granite porphyry) were carried out by means of LA-ICP-MS at the Key Laboratory of Isotope Geochronology and Geochemistry, Guangzhou Institute of Geochemistry, CAS. A Resolution M-50 laser-ablation system was used in conjunction with an Agilent 7500 ICP-MS. The clearest, least fractured rims of the zircon crystals were selected as suitable targets for laser ablation analyses. Sample mounts were placed in the two-volume sample cell flushed with Ar and He. Laser ablation was operated at a constant energy 80 mJ and at 8 Hz, with a spot diameter of 31 μm . The ablated material was carried by the He gas to the Agilent 7500 ICP-MS. Element corrections were made for mass bias drift, which was evaluated by reference to standard glass NIST 610 (Y.S. Liu et al., 2008). The Temora was used as the age standard ($^{206}\text{Pb}/^{238}\text{U} = 416.8 \text{ Ma}$) (Black et al., 2003). Trace element concentrations were obtained by normalizing count rates for each analyzed element to those for Si, and assuming SiO_2 to be stoichiometric in zircon (Tu et al., 2011).

Molybdenite separates were obtained by crushing the samples in a porcelain mill, gravity sorting, electromagnetic separation, and finally hand-picking under a binocular microscope (purity >99%). Molybdenite dissolution and preparation were performed at the Key Laboratory of Isotope Geochronology and Geochemistry, Guangzhou Institute of Geochemistry. The Re and Os concentration and isotopic composition were measured using a X-7 Inductively Coupled Plasma Mass Spectrometer (ICP-MS) at the College of Resource Science, University of Chang'an, using a type of XSeries-7 quadrupole ICP-MS (Thermo Scientific, USA) with glass spray chamber and concentric glass nebulizer. Details of the

analytical procedures were given by Sun et al. (2010). Model ages were calculated following the equation: $t = [\ln(1 + ^{187}\text{Os}/^{187}\text{Re})]/\lambda$, where λ is the decay constant of ^{187}Re , $1.666 \times 10^{-11}/\text{yr}^{-1}$ (Smoliar et al., 1996). Uncertainties in spike calibration, weighing for spike and sample, and mass spectrometry measurements for isotope ratio and mass fractionation factor and the decay constant of ^{187}Re are considered (Sun et al., 2010). All uncertainties are given as absolute amounts at the 2σ level.

The whole-rock Sr–Nd–Pb isotopic analyses were performed at the State Key Laboratory of Isotope Geochemistry, Guangzhou Institute of Geochemistry, CAS. Powders of samples were dissolved in HF– HClO_4 for Sr and Nd isotope analyses and in HF– HNO_3 for Pb isotope analyses. Dissolution was at 200 $^\circ\text{C}$ for one week. The isotope measurements were performed on a Neptune Plus multi-collection mass spectrometry equipped with nine Faraday cup collectors and eight ion counters. Details of Sr, Nd, and Pb isotopic analytical methods are similar to Waight et al. (2002), Y.H. Yang et al. (2010), and Chernyshev et al. (2007). Normalizing factors used to correct the mass fractionation of Sr and Nd during the measurements were $^{86}\text{Sr}/^{88}\text{Sr} = 0.1194$ and $^{146}\text{Nd}/^{144}\text{Nd} = 0.7219$. Analyses of standards NIST SRM 987 and the Shin Etsu JNdi-1 over the measurement period provided $^{87}\text{Sr}/^{86}\text{Sr} = 0.710280 \pm 6$ (2σ , $n = 15$) and $^{143}\text{Nd}/^{144}\text{Nd} = 0.512087 \pm 2$ (2σ , $n = 18$), respectively. Samples for Pb isotope analyses were doped with Tl and mass discrimination was corrected relative to a certified $^{205}\text{Tl}/^{203}\text{Tl}$ ratio. Analyses of standard NIST SRM 981, over the measurement period provided $^{206}\text{Pb}/^{204}\text{Pb} = 16.935 \pm 1$ (2σ , $n = 16$), $^{207}\text{Pb}/^{204}\text{Pb} = 15.486 \pm 1$ (2σ , $n = 16$), and $^{208}\text{Pb}/^{204}\text{Pb} =$

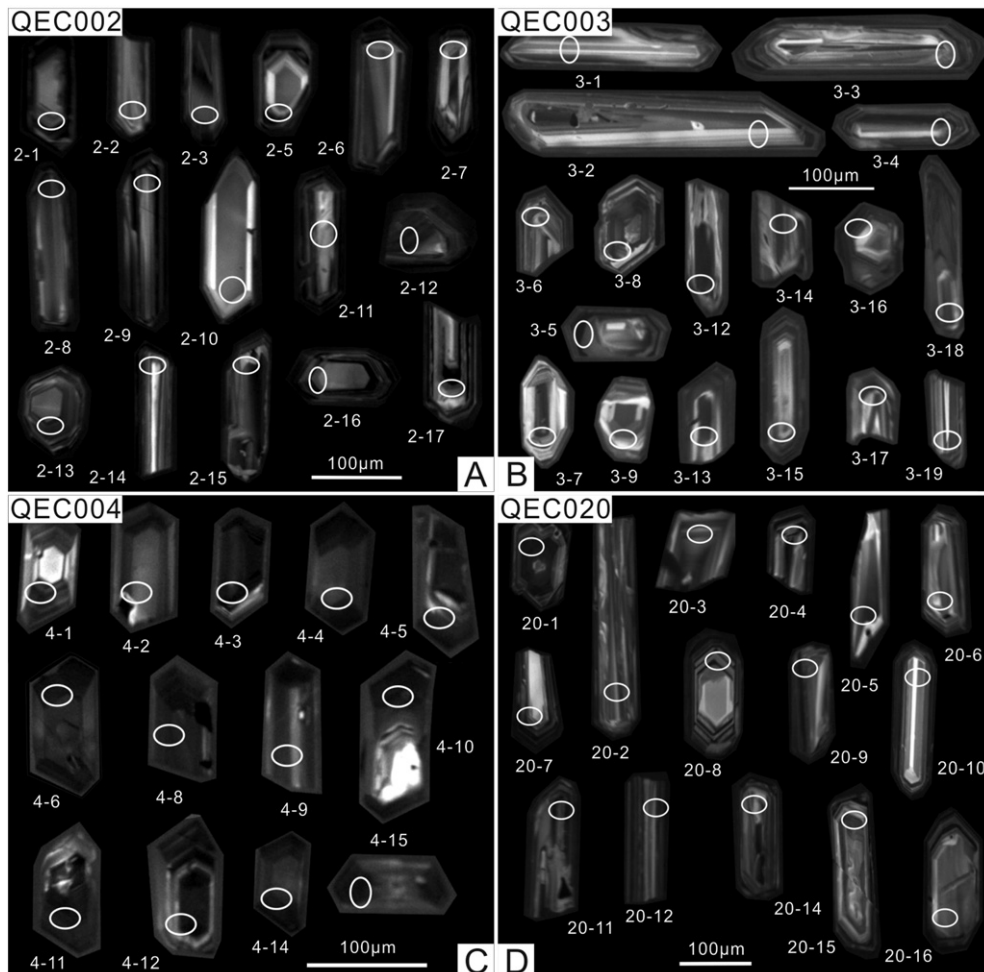


Fig. 7. Cathodoluminescent images of zircon grains of the dated samples from the Qian'echong porphyry Mo deposit, showing the locations of analyzed points.

36.676 ± 1 (2σ , $n = 16$). Analytical errors for Sr, Nd, and Pb isotopic ratios are given as 2σ .

5. Analytical results

5.1. Geochemical composition

Analytical results of major and trace elements of igneous rocks at the Qian'echong deposit are presented in Table 1. Samples QEC002, QEC003,

and QEC004 have high SiO_2 (76.46–77.21%); low TFe_2O_3 (0.55–1.15%), CaO (0.04–0.07%), Na_2O (0.01–2.09%), and P_2O_5 (0.010–0.027%); and a high $\text{K}_2\text{O}/\text{Na}_2\text{O}$ ratio (>2.5) (Table 1). Sample QEC004 also has a very low content of MgO .

The granite porphyry stock and dike samples (QEC005, QEC006, QEC008–QEC012, QEC014–QEC016, and QEC018–QEC020) have similar features, with high SiO_2 (72.38–73.35%), alkalis ($\text{Na}_2\text{O} + \text{K}_2\text{O} = 8.13$ –9.03%), and Al_2O_3 (13.89–14.82%); and low TiO_2 (0.187–0.237%), MgO (0.341–0.413%), and CaO (0.91–1.36%). The values of $\text{K}_2\text{O}/\text{Na}_2\text{O}$,

Table 2

Results of SIMS U–Pb dating for the single-grain zircon from the rhyolite porphyry dike (QEC003), quartz porphyry dike (QEC004) and granite porphyry dike (QEC002, QEC020).

Spot no.	Content ($\mu\text{g}/\text{g}$)			Ratios							Age (Ma)						
	U	Th	Pb	Th/U	$^{207}\text{Pb}/^{235}\text{U}$	$\pm\%$	$^{206}\text{Pb}/^{238}\text{U}$	$\pm\%$	Error correct	$^{207}\text{Pb}/^{206}\text{Pb}$	$\pm\%$	$^{206}\text{Pb}/^{238}\text{U}$	1σ	$^{207}\text{Pb}/^{235}\text{U}$	1σ	$^{207}\text{Pb}/^{206}\text{Pb}$	1σ
QEC002-1	457	198	11	0.43	0.1317	4.12	0.0197	1.68	0.41	0.0486	3.76	125.5	2.1	125.7	4.9	129.0	86.2
QEC002-2	253	397	8	1.57	0.1352	3.71	0.0201	1.58	0.43	0.0488	3.35	128.3	2.0	128.7	4.5	136.2	76.9
QEC002-3	486	424	13	0.87	0.1313	3.40	0.0202	1.55	0.46	0.0472	3.02	128.6	2.0	125.3	4.0	61.8	70.5
QEC002-5	275	452	8	1.64	0.1399	3.51	0.0199	1.53	0.43	0.0509	3.16	127.2	1.9	132.9	4.4	237.0	71.4
QEC002-6	264	361	8	1.37	0.1283	5.68	0.0200	1.60	0.28	0.0467	5.45	127.4	2.0	122.6	6.6	31.5	125.6
QEC002-7	500	739	15	1.48	0.1318	3.35	0.0201	1.51	0.45	0.0476	2.99	128.3	1.9	125.8	4.0	77.5	69.6
QEC002-8	550	628	15	1.14	0.1323	4.59	0.0198	1.54	0.33	0.0484	4.33	126.6	1.9	126.2	5.5	117.8	99.0
QEC002-9	459	431	12	0.94	0.1322	2.99	0.0197	1.51	0.50	0.0487	2.58	125.7	1.9	126.0	3.5	133.4	59.5
QEC002-10	178	337	6	1.89	0.1296	4.98	0.0193	1.63	0.33	0.0488	4.70	123.0	2.0	123.7	5.8	137.3	106.9
QEC002-11	446	348	11	0.78	0.1215	7.50	0.0196	1.61	0.22	0.0448	7.32	125.4	2.0	116.4	8.3	64.9	169.7
QEC002-12	770	616	20	0.80	0.1363	2.40	0.0205	1.50	0.63	0.0483	1.87	130.6	1.9	129.7	2.9	114.6	43.6
QEC002-13	753	383	18	0.51	0.1274	2.71	0.0197	1.52	0.56	0.0470	2.25	125.6	1.9	121.8	3.1	46.8	52.8
QEC002-14	281	437	8	1.56	0.1229	4.76	0.0200	1.52	0.32	0.0446	4.51	127.6	1.9	117.7	5.3	78.0	106.9
QEC002-15	500	1031	16	2.06	0.1313	3.31	0.0198	1.52	0.46	0.0482	2.94	126.1	1.9	125.3	3.9	109.4	68.1
QEC002-16	928	794	25	0.86	0.1399	2.35	0.0203	1.51	0.64	0.0500	1.80	129.4	1.9	133.0	2.9	196.8	41.3
QEC002-17	1239	1362	36	1.10	0.1417	2.42	0.0210	1.53	0.63	0.0489	1.88	134.0	2.0	134.6	3.1	145.1	43.6
QEC003-1	188	379	6	2.02	0.1322	3.97	0.0197	1.61	0.41	0.0487	3.62	125.7	2.0	126.1	4.7	132.8	83.1
QEC003-2	346	137	8	0.40	0.1282	3.98	0.0200	1.52	0.38	0.0466	3.67	127.4	1.9	122.4	4.6	28.2	85.8
QEC003-3	581	1377	20	2.37	0.1321	2.89	0.0197	1.53	0.53	0.0486	2.46	125.9	1.9	126.0	3.4	128.6	56.8
QEC003-4	414	380	11	0.92	0.1294	4.46	0.0206	1.58	0.35	0.0455	4.17	131.6	2.1	123.5	5.2	29.3	98.1
QEC003-5	547	230	13	0.42	0.1326	2.68	0.0198	1.54	0.57	0.0487	2.20	126.2	1.9	126.4	3.2	131.7	50.9
QEC003-6	357	209	9	0.59	0.1259	3.10	0.0200	1.55	0.50	0.0457	2.68	127.5	2.0	120.4	3.5	16.5	63.5
QEC003-7	664	633	18	0.95	0.1397	3.92	0.0198	1.53	0.39	0.0511	3.61	126.6	1.9	132.8	4.9	245.7	81.1
QEC003-8	682	688	19	1.01	0.1309	2.83	0.0201	1.52	0.54	0.0474	2.39	128.0	1.9	124.9	3.3	67.4	55.9
QEC003-9	628	420	16	0.67	0.1296	2.75	0.0200	1.53	0.56	0.0470	2.29	127.7	1.9	123.7	3.2	49.1	53.7
QEC003-12	2419	2928	69	1.21	0.1323	1.88	0.0199	1.51	0.80	0.0482	1.12	127.1	1.9	126.2	2.2	108.3	26.3
QEC003-13	590	661	16	1.12	0.1324	3.04	0.0200	1.53	0.50	0.0480	2.62	127.6	1.9	126.3	3.6	101.6	60.9
QEC003-14	842	1701	28	2.02	0.1333	3.01	0.0197	1.54	0.51	0.0490	2.58	125.9	1.9	127.1	3.6	148.1	59.5
QEC003-15	607	730	17	1.20	0.1351	2.56	0.0199	1.53	0.60	0.0491	2.05	127.3	1.9	128.7	3.1	154.1	47.4
QEC003-16	704	397	18	0.56	0.1330	2.80	0.0204	1.52	0.54	0.0472	2.35	130.4	2.0	126.8	3.3	60.0	55.2
QEC003-17	790	930	23	1.18	0.1377	2.73	0.0199	1.52	0.56	0.0501	2.26	127.2	1.9	131.0	3.4	199.9	51.8
QEC003-18	1242	782	31	0.63	0.1305	3.84	0.0199	1.52	0.40	0.0476	3.53	127.0	1.9	124.6	4.5	78.3	81.8
QEC003-19	399	803	13	2.01	0.1264	3.74	0.0200	1.65	0.44	0.0457	3.36	127.9	2.1	120.8	4.3	16.0	79.2
QEC004-1	471	1190	17	2.52	0.1327	3.49	0.0201	1.54	0.44	0.0479	3.12	128.3	2.0	126.5	4.2	93.3	72.4
QEC004-2	750	1333	24	1.78	0.1299	2.60	0.0201	1.54	0.59	0.0469	2.10	128.3	2.0	124.0	3.0	42.7	49.4
QEC004-3	2649	7221	97	2.73	0.1243	9.15	0.0201	1.60	0.18	0.0449	9.01	128.1	2.0	119.0	10.3	59.8	206.2
QEC004-4	1217	1078	33	0.89	0.1338	2.19	0.0203	1.51	0.69	0.0478	1.58	129.6	1.9	127.5	2.6	88.9	37.1
QEC004-5	1101	821	28	0.75	0.1331	2.28	0.0201	1.58	0.69	0.0481	1.65	128.2	2.0	126.9	2.7	102.4	38.6
QEC004-6	2223	3431	68	1.54	0.1324	3.50	0.0203	1.50	0.43	0.0472	3.17	129.8	1.9	126.3	4.2	60.6	73.8
QEC004-8	1386	2600	46	1.88	0.1411	2.52	0.0203	1.52	0.60	0.0503	2.02	129.8	2.0	134.0	3.2	208.9	46.1
QEC004-9	1067	1611	32	1.51	0.1350	2.43	0.0201	1.53	0.63	0.0486	1.88	128.6	1.9	128.6	2.9	129.1	43.7
QEC004-10	1936	2618	58	1.35	0.1351	2.02	0.0204	1.53	0.76	0.0479	1.32	130.5	2.0	128.7	2.4	95.3	30.9
QEC004-11	1997	2734	59	1.37	0.1347	11.92	0.0202	1.59	0.13	0.0484	11.81	128.9	2.0	128.3	14.5	117.4	257.1
QEC004-12	1272	2660	43	2.09	0.1380	4.98	0.0204	1.51	0.30	0.0491	4.74	130.0	1.9	131.3	6.1	154.1	107.4
QEC004-14	1452	1639	39	1.13	0.1254	7.04	0.0198	1.56	0.22	0.0459	6.86	126.5	2.0	120.0	8.0	7.9	157.9
QEC004-15	2414	4765	79	1.97	0.1325	2.27	0.0203	1.98	0.87	0.0474	1.11	129.3	2.5	126.3	2.7	70.5	26.2
QEC020-1	1213	787	31	0.65	0.1392	2.75	0.0205	2.24	0.82	0.0493	1.59	130.7	2.9	132.3	3.4	160.9	36.7
QEC020-2	310	441	9	1.42	0.1320	3.59	0.0199	2.27	0.63	0.0482	2.78	126.7	2.9	125.9	4.3	109.0	64.3
QEC020-3	298	236	8	0.79	0.1226	9.14	0.0196	2.21	0.24	0.0454	8.87	125.0	2.7	117.5	10.2	32.0	202.2
QEC020-4	933	974	27	1.04	0.1409	2.89	0.0202	2.21	0.76	0.0506	1.87	128.9	2.8	133.8	3.6	222.2	42.6
QEC020-5	434	165	10	0.38	0.1285	3.25	0.0198	2.21	0.68	0.0470	2.38	126.7	2.8	122.7	3.8	46.8	56.0
QEC020-6	376	1146	15	3.05	0.1223	5.62	0.0196	2.23	0.40	0.0453	5.16	125.1	2.8	117.2	6.2	39.7	120.7
QEC020-7	182	202	5	1.11	0.1318	6.00	0.0200	2.29	0.38	0.0478	5.55	127.5	2.9	125.7	7.1	91.5	126.4
QEC020-8	546	260	13	0.48	0.1312	3.83	0.0200	2.21	0.58	0.0476	3.13	127.6	2.8	125.2	4.5	79.3	72.8
QEC020-9	1141	1139	32	1.00	0.1362	2.84	0.0204	2.21	0.78	0.0485	1.79	130.0	2.8	129.6	3.5	122.1	41.7
QEC020-10	112	151	3	1.35	0.1293	5.22	0.0200	2.29	0.44	0.0468	4.69	128.0	2.9	123.5	6.1	38.4	108.7
QEC020-11	518	272	12	0.52	0.1314	3.75	0.0193	2.31	0.62	0.0495	2.96	122.9	2.8	125.3	4.4	171.0	67.6
QEC020-12	1393	1569	38	1.13	0.1313	2.68	0.0195	2.21	0.82	0.0489	1.52	124.4	2.7	125.3	3.2	141.4	35.2
QEC020-14	469	344	12	0.73	0.1321	3.20	0.0198	2.22	0.69	0.0483	2.30	126.5	2.8	126.0	3.8	115.7	53.4
QEC020-15	617	304	14	0.49	0.1283	3.68	0.0193	2.28	0.62	0.0483	2.88	123.0	2.8	122.6	4.3	113.6	66.7
QEC020-16	328	443	10	1.35	0.1260	4.00	0.0199	2.20	0.55	0.0460	3.34	126.9	2.8	120.5	4.6	4.2	78.7

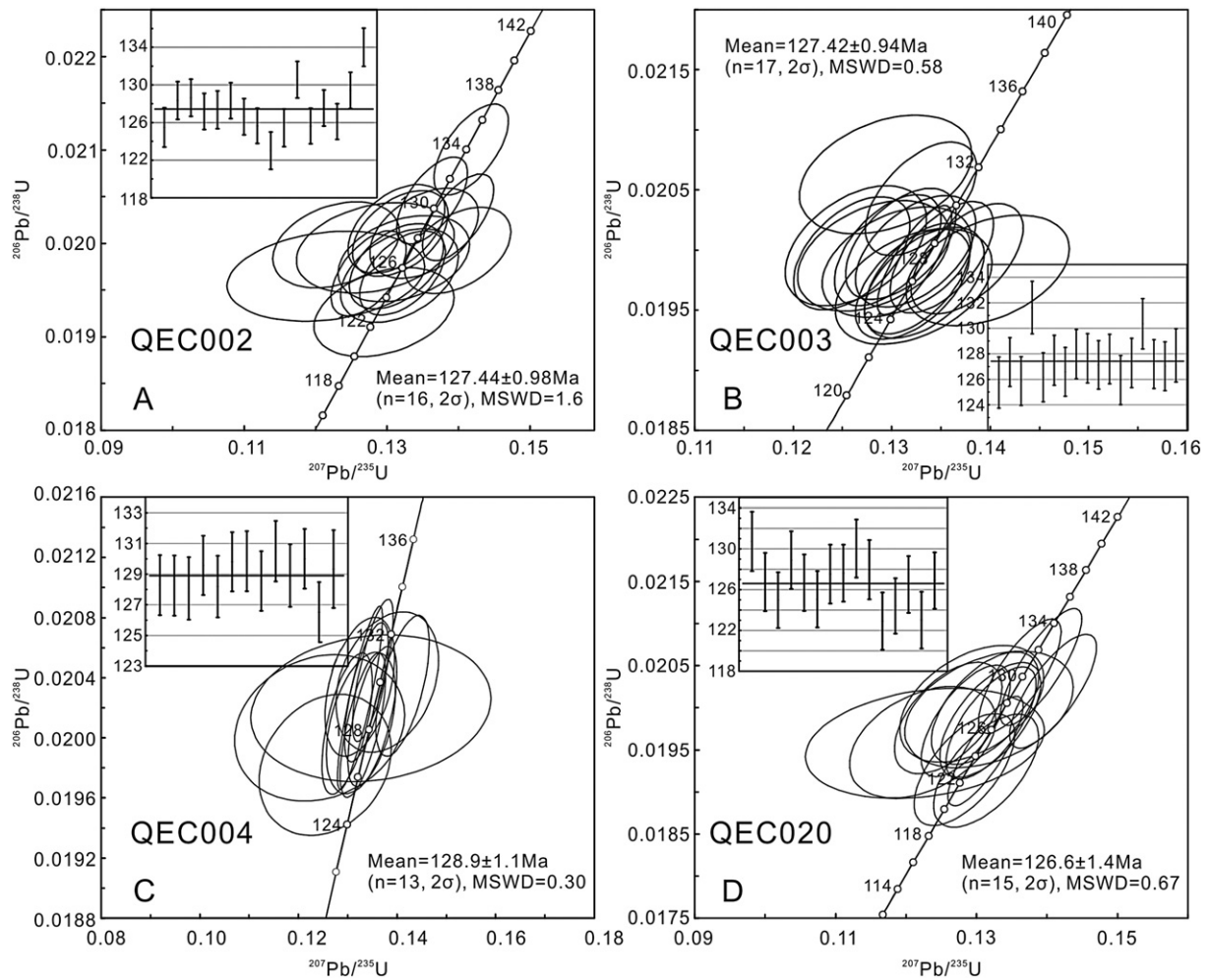


Fig. 8. The SIMS zircon U-Pb concordia diagrams for the porphyry dikes at Qian'echong.

A/CNK, and Mg# are 1.3–1.4, 1.03–1.09, and 33–44, respectively. All samples cluster in the high-K calc-alkaline to shoshonite fields in a K_2O-SiO_2 plot (Fig. 5A) or in the peraluminous field in an A/NK–A/CNK diagram (Fig. 5B). The geochemical characteristics suggest that the Qian'echong granite porphyries belong to the peraluminous high-K calc-alkaline to shoshonite series.

All studied samples show steep LREE and flat HREE patterns in a chondrite-normalized REE diagram (Fig. 6A). They exhibit strong peaks for Rb, Th, U, K, Zr, and Hf, and troughs for Eu, Nb, Ta, Sr, Ba, P, and Ti in a primitive mantle-normalized trace element diagram (Fig. 6B). The buried biotite granite porphyries have higher $\Sigma REE + Y$ contents of 164.53 to 215.62 ppm, δEu values of 0.62 to 0.81, and $(La/Yb)_N$ ratios of

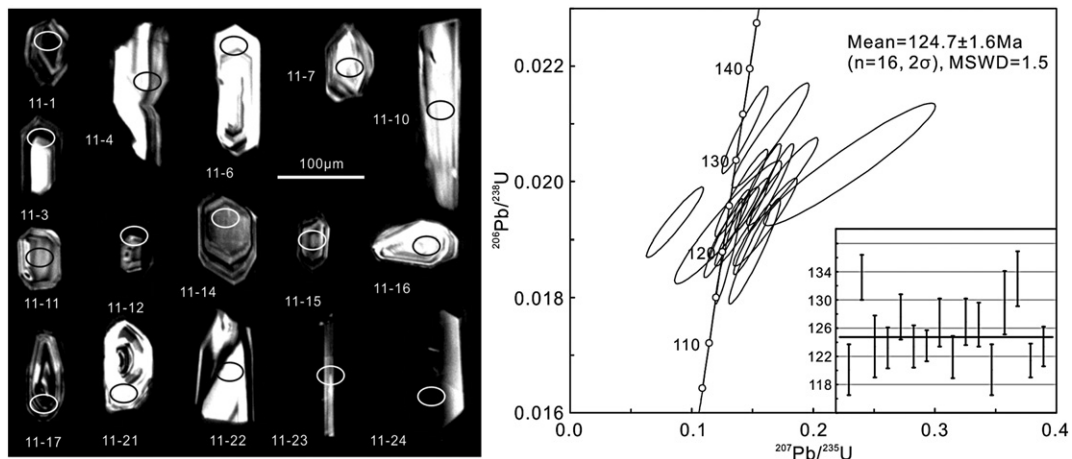


Fig. 9. Cathodoluminescent images and LA-ICPMS zircon U-Pb concordia diagram for the porphyry stock (QEC011) at Qian'echong.

Table 3

Results of LA-ICPMS U–Pb dating for the single-grain zircon from biotite granite porphyry stock (QEC011) at Qian'echong.

Spot no.	Content (μg/g)		Ratios					Age (Ma)								
	U	Th	Pb	Th/U	²⁰⁶ Pb/ ²³⁸ U	1σ	²⁰⁷ Pb/ ²³⁵ U	1σ	²⁰⁷ Pb/ ²⁰⁶ Pb	1σ	²⁰⁶ Pb/ ²³⁸ U	1σ	²⁰⁷ Pb/ ²³⁵ U	1σ	²⁰⁷ Pb/ ²⁰⁶ Pb	1σ
QEC011-01	1348	701	32	0.52	0.0188	0.0006	0.1305	0.0074	0.0507	0.0026	120.1	3.6	124.6	6.6	233.4	118.5
QEC011-03	621	793	18	1.28	0.0209	0.0005	0.1438	0.0125	0.0506	0.0044	133.2	3.2	136.5	11.1	220.4	6.5
QEC011-04	127	237	4	1.87	0.0193	0.0007	0.1300	0.0291	0.0516	0.0114	123.4	4.4	124.1	26.2	333.4	375.9
QEC011-06	291	272	8	0.94	0.0193	0.0005	0.1414	0.0147	0.0543	0.0058	123.2	2.9	134.3	13.1	383.4	244.4
QEC011-07	249	425	8	1.71	0.02	0.0005	0.1744	0.0194	0.0649	0.0074	127.6	3.2	163.2	16.8	772.2	236.1
QEC011-10	296	371	8	1.25	0.0193	0.0005	0.1605	0.0173	0.0604	0.0061	123.4	3.0	151.2	15.1	620.4	225.0
QEC011-11	440	523	12	1.19	0.0193	0.0004	0.1349	0.0135	0.0501	0.0051	123.5	2.2	128.5	12.1	198.2	218.5
QEC011-12	1176	1717	30	1.46	0.0199	0.0005	0.1651	0.0123	0.0601	0.0042	126.8	3.4	155.2	10.7	607.1	149.1
QEC011-14	955	812	23	0.85	0.0191	0.0005	0.1290	0.0124	0.0476	0.0043	121.9	3.0	123.2	11.1	79.7	196.3
QEC011-15	878	1585	26	1.80	0.0199	0.0005	0.1545	0.0125	0.0557	0.0044	126.9	3.3	145.9	11	442.6	174.1
QEC011-16	393	705	13	1.79	0.0198	0.0005	0.1409	0.0143	0.0517	0.0054	126.5	3.1	133.9	12.7	272.3	238.9
QEC011-17	1231	703	27	0.57	0.0188	0.0006	0.1517	0.014	0.0574	0.0048	120.1	3.6	143.4	12.3	505.6	185.9
QEC011-21	334	606	10	1.82	0.0203	0.0007	0.2298	0.0466	0.0734	0.0119	129.6	4.5	210	38.5	1025.6	333.3
QEC011-22	216	216	6	1.00	0.0208	0.0006	0.1648	0.021	0.0605	0.0074	133.0	3.9	154.9	18.3	620.4	268.5
QEC011-23	854	494	20	0.58	0.019	0.0004	0.1498	0.0101	0.0573	0.0037	121.4	2.4	141.7	8.9	501.9	142.6
QEC011-24	232	661	9	2.85	0.0193	0.0004	0.0862	0.0155	0.0331	0.0058	123.4	2.8	84.0	14.5	Error	Error

29.71 to 82.83, relative to the more shallowly emplaced rhyolite to granite and quartz porphyry dikes (Table 1).

5.2. SIMS zircon U–Pb ages

Zircon CL images of the samples QEC002 (Fig. 7A), QEC003 (Fig. 7B), QEC004 (Fig. 7C), and QEC020 (Fig. 7D) show that the majority of zircon grains are magmatic in origin. They are generally transparent, euhedral, 50- to 300-μm-long, and elongated in shape, with aspect ratios (length/width) of 2–3.5, and show clearly concentric oscillating zones. With common lead correction, Pb/Pb ages are suitable for the >1 Ga zircon grains, and the Pb/U ages are more suitable for the <1 Ga zircons (Anderson, 2002).

Zircon grains from the surface granite porphyry dike (QEC002) have U, Th, and common Pb contents of 178–1239 ppm, 198–1362 ppm, and 6–36 ppm, respectively (Table 2). In the ²⁰⁶Pb/²³⁸U–²⁰⁷Pb/²³⁵U concordia diagram, the 16 analytical spots concentrate in a small region near the concordia line (Fig. 8A), and yield a weighted average ²⁰⁶Pb/²³⁸U age of 127.44 ± 0.98 Ma (MSWD = 1.6, 2σ).

The analyses of 17 zircon grains from the rhyolitic porphyry dike (QEC003) show U and Th concentrations of 188 to 2419 ppm and 137 to 2928 ppm, respectively, with Th/U ratios ranging from 0.40 to 2.37. Their common Pb concentrations are 6 to 69 ppm. All the analyses plot in a small region near the concordia line (Fig. 8B), and yield a weighted average ²⁰⁶Pb/²³⁸U age of 127.42 ± 0.94 Ma (MSWD = 0.58, 2σ), similar to the age of the sample of the granite porphyry dike.

The U and Th concentrations of 13 zircon grains from the quartz porphyry dike (QEC004) range from 471–2649 ppm and 821–7221 ppm, respectively. These values are generally higher than those of samples QEC002, QEC003, and QEC020 (Table 2). Within analytical precision, the ratios of ²⁰⁶Pb/²³⁸U and ²⁰⁷Pb/²³⁵U agree internally (Fig. 8C), and yield a weighted average ²⁰⁶Pb/²³⁸U age of 128.9 ± 1.1 Ma (MSWD = 0.30, 2σ), which is slightly older than the other samples.

The analyses of 15 zircon grains from the deeper granite porphyry dike (QEC020) indicated U and Th concentrations are similar to those

of zircons from samples QEC002 and QEC003, with U = 112–1393 ppm, Th = 151–1569 ppm, and Th/U = 0.28–3.05. All spots concentrate in a small region near the concordia line (Fig. 8D), and yield a weighted average ²⁰⁶Pb/²³⁸U age of 126.6 ± 1.4 Ma (MSWD = 0.67, 2σ), overlapping, within error, the ages of the surface rhyolite and granite porphyry dikes.

5.3. LA-ICP-MS zircon U–Pb dating

Zircon grains from the buried biotite granite porphyry stock (QEC011) are colorless transparent, and elongated, prismatic and euhedral in shape, with lengths of 50–250 μm and aspect ratios of 2:1 to 4:1. They have oscillatory zoning (Fig. 9), with some showing corroded edges. The 16 analyses (Table 3) concentrate in a small region near the concordia line (Fig. 9), and yield a weighted average ²⁰⁶Pb/²³⁸U age of 124.7 ± 1.6 Ma (MSWD = 1.5, 2σ), which, within error, is same to the SIMS zircon U–Pb age of 126.6 ± 1.4 Ma obtained from the buried biotite granite porphyry dike.

5.4. Molybdenite Re–Os dating

Six Re–Os analyses of five molybdenite samples are presented in Table 4. Total Re and ¹⁸⁷Os concentrations range from 7.2589 to 14.268 ppm and from 9.6050 to 18.517 ppb, respectively. The individual ages range from 123.31 ± 1.02 Ma to 128.49 ± 1.40 Ma, yielding an isochron age of 126 ± 11 Ma (MSWD = 11.1) and a weighted average age of 125.3 ± 1.7 Ma (MSWD = 8.9) (Fig. 10). Because the minimum age (123.31 ± 1.02 Ma) is inconsistent with the maximum age (128.49 ± 1.40 Ma) within analytical error, the molybdenite may have crystallized heterogeneously and the isochron age cannot be accepted as representative of the crystallization age of the molybdenite. Consequently, all the individual ages are interpreted here to represent discrete, best estimate crystallization ages for each molybdenite sample; and the weighted average age might represent the peak-crystallization time of molybdenite.

Table 4

Results of the Re–Os dating of molybdenite from the Qian'echong Mo deposit.

Sample	Weight (g)	Re (μg/g)	2σ	¹⁸⁷ Re (μg/g)	2σ	¹⁸⁷ Os (ng/g)	2σ	Age (Ma)	2σ
402-1	0.1013	7.2589	0.0300	4.5625	0.0188	9.6050	0.0509	126.23	0.85
402-2	0.1015	14.268	0.0380	8.9679	0.0239	18.517	0.2290	123.81	1.56
005-1	0.0999	10.702	0.0526	6.7269	0.0330	14.026	0.0871	125.02	0.99
005-1	0.1009	11.623	0.0613	7.3058	0.0385	15.264	0.0851	125.28	0.96
005-2	0.1013	7.5558	0.0357	4.7491	0.0224	9.7661	0.0664	123.31	1.02
005-3	0.1022	12.329	0.0406	7.7493	0.0256	16.607	0.1720	128.49	1.40

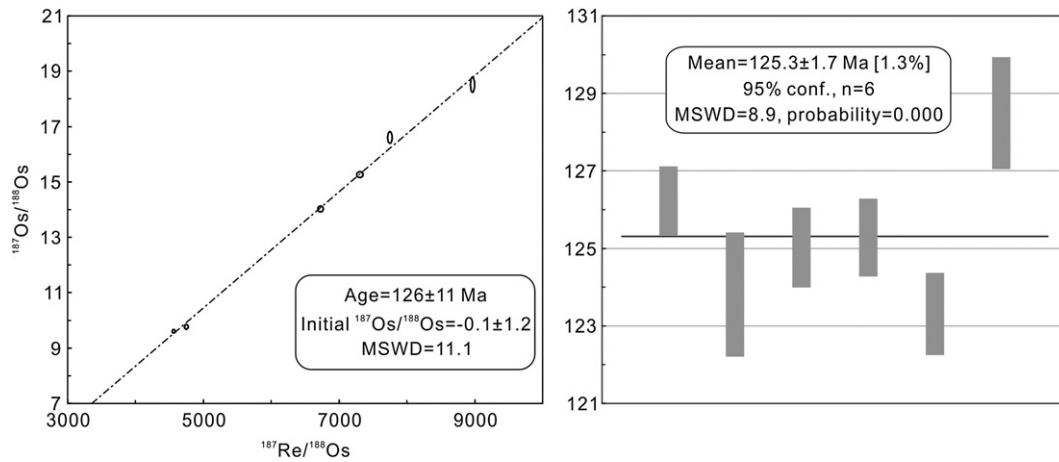


Fig. 10. Molybdenite Re–Os isochron age and weighted average age for the Qian'echong porphyry Mo deposit.

5.5. Whole-rock Sr–Nd–Pb isotopic compositions

Whole-rock Sr–Nd–Pb isotopic compositions of the intrusive rocks at the Qian'echong deposit are presented in Table 5. The ratios of $^{87}\text{Rb}/^{86}\text{Sr}$, $^{147}\text{Sm}/^{144}\text{Nd}$, $^{238}\text{U}/^{204}\text{Pb}$, $^{235}\text{U}/^{204}\text{Pb}$, and $^{232}\text{Th}/^{204}\text{Pb}$ were calculated using the Rb, Sr, Sm, Nd, U, Th, and Pb concentrations obtained by ICP-MS and the measured isotope ratios of the samples. The I_{Sr} represents the initial $^{87}\text{Sr}/^{86}\text{Sr}$ ratio when the rock formed, using $\lambda_{\text{Rb}} = 1.42 \times 10^{-11} \text{ a}^{-1}$ (Steiger and Jager, 1977). $\epsilon_{\text{Nd}}(t)$ was calculated using $(^{143}\text{Nd}/^{144}\text{Nd})_{\text{CHUR}} = 0.512638$, $(^{147}\text{Sm}/^{144}\text{Nd})_{\text{CHUR}} = 0.1967$ (Jacobsen and Wasserburg, 1980) and $\lambda_{\text{Sm}} = 6.54 \times 10^{-12} \text{ a}^{-1}$ (Lugmair and Marti, 1978). $T_{\text{DM1}}(\text{Nd})$ was calculated using $(^{143}\text{Nd}/^{144}\text{Nd})_{\text{DM}} = 0.51315$ and $(^{147}\text{Sm}/^{144}\text{Nd})_{\text{DM}} = 0.2137$ (Peucat et al., 1988). $T_{\text{DM2}}(\text{Nd}) = T_{\text{DM1}} - (T_{\text{DM1}} - t) \times [(f_{\text{CC}} - f_{\text{S}}) / (f_{\text{CC}} - f_{\text{DM}})]$, where $f_{\text{S}} = [(^{147}\text{Sm}/^{144}\text{Nd})_{\text{S}} - (^{147}\text{Sm}/^{144}\text{Nd})_{\text{CHUR}}] - 1$, $f_{\text{DM}} = [(^{147}\text{Sm}/^{144}\text{Nd})_{\text{DM}} - (^{147}\text{Sm}/^{144}\text{Nd})_{\text{CHUR}}] - 1$, $f_{\text{CC}} = -0.4$ (DePaolo

and Wasserburg, 1979). $(^{147}\text{Sm}/^{144}\text{Nd})_{\text{S}}$ is the calculated ratio of sample. The $(^{206}\text{Pb}/^{204}\text{Pb})_{\text{t}}$, $(^{207}\text{Pb}/^{204}\text{Pb})_{\text{t}}$, and $(^{208}\text{Pb}/^{204}\text{Pb})_{\text{t}}$ present initial Pb isotopic ratios when the rock formed, calculated using a single-stage model. Ages of these samples used for the calculations are given in Sections 5.2 and 5.3.

The rhyolite porphyry and quartz porphyry dikes have high $^{87}\text{Rb}/^{86}\text{Sr}$ values of 12.08 and 10.68, with I_{Sr} values of 0.70901 and 0.71788, respectively. They have nearly identical $\epsilon_{\text{Nd}}(t)$ values of -16.4 and -16.2 , and $T_{\text{DM2}}(\text{Nd})$ ages of 2.25 Ga and 2.24 Ga. The $(^{206}\text{Pb}/^{204}\text{Pb})_{\text{t}}$, $(^{207}\text{Pb}/^{204}\text{Pb})_{\text{t}}$, and $(^{208}\text{Pb}/^{204}\text{Pb})_{\text{t}}$ of the rhyolite porphyry and quartz porphyry dikes are 16.562 and 16.701, 15.347 and 15.368, and 37.098 and 37.578, respectively.

The biotite granite porphyry stock samples have $^{87}\text{Rb}/^{86}\text{Sr}$ values of 1.73–2.65, with I_{Sr} values ranging from 0.70770 to 0.70901. Their $\epsilon_{\text{Nd}}(t)$ values range from -26.1 to -17.8 , with $T_{\text{DM1}}(\text{Nd})$ of 1.96–2.24 Ga and $T_{\text{DM2}}(\text{Nd})$ of 2.36–3.03 Ga. Compared to the biotite granite porphyry

Table 5

Whole-rock Sr–Nd–Pb isotopic compositions of the intrusions at Qian'echong deposit.

Sample No.	QEC003	QEC004	QEC005	QEC008	QEC010	QEC011	QEC012	QEC014	QEC018	QEC019	QEC020
t/Ma	127.4	128.9	124.7	124.7	124.7	124.7	124.7	124.7	126.6	126.6	126.6
Rb/ppm	273.9	300.8	182.0	176.3	185.3	193.6	197.1	230.2	259.3	239.7	201.1
Sr/ppm	65.6	81.5	303.7	284.1	251.2	263.3	275.3	250.7	244.1	241.6	229.1
$^{87}\text{Rb}/^{86}\text{Sr}$	12.08	10.68	1.73	1.79	2.13	2.12	2.07	2.65	3.07	2.87	2.54
$^{87}\text{Sr}/^{86}\text{Sr}$	0.730892	0.737452	0.711522	0.711282	0.711480	0.711984	0.712378	0.713708	0.713199	0.712599	0.711846
2σ	0.000006	0.000006	0.000007	0.000005	0.000006	0.000005	0.000006	0.000005	0.000006	0.000005	0.000006
I_{Sr}	0.70901	0.71788	0.70846	0.70811	0.70770	0.70822	0.70871	0.70901	0.70768	0.70744	0.70729
Sm/ppm	2.10	3.87	3.75	3.52	4.16	3.70	3.54	3.44	3.35	3.71	3.39
Nd/ppm	14.07	18.64	28.66	25.98	25.84	25.74	27.66	25.37	23.08	25.88	23.62
$^{147}\text{Sm}/^{144}\text{Nd}$	0.0901	0.1255	0.0791	0.0818	0.0972	0.0869	0.0774	0.0819	0.0878	0.0867	0.0868
$^{143}\text{Nd}/^{144}\text{Nd}$	0.511711	0.511746	0.511211	0.511434	0.511645	0.511499	0.511226	0.511208	0.511661	0.511679	0.511657
2σ	0.000004	0.000003	0.000004	0.000003	0.000003	0.000004	0.000004	0.000004	0.000004	0.000003	0.000003
$\epsilon_{\text{Nd}}(t)$	-16.4	-16.2	-26.0	-21.7	-17.8	-20.5	-25.6	-26.1	-17.3	-16.9	-17.4
T_{DM1}/Ga	1.77	2.42	2.19	1.98	1.96	1.98	2.14	2.24	1.80	1.76	1.79
T_{DM2}/Ga	2.25	2.24	3.02	2.67	2.36	2.57	2.99	3.03	2.32	2.29	2.33
U/ppm	6.63	2.70	4.98	8.18	7.60	6.97	3.15	4.39	8.33	7.80	8.33
Th/ppm	28.5	13.2	23.1	22.2	23.4	23.6	24.3	23.4	27.3	25.5	29.1
Pb/ppm	13.0	54.1	35.6	32.2	31.0	29.0	33.6	32.1	233.2	98.9	25.4
$^{206}\text{Pb}/^{204}\text{Pb}$	17.1931	16.7624	16.1824	16.3982	16.4355	16.5592	16.2005	16.4677	16.6239	16.6804	16.9395
2σ	0.0003	0.0002	0.0002	0.0002	0.0003	0.0002	0.0002	0.0002	0.0002	0.0002	0.0003
$^{207}\text{Pb}/^{204}\text{Pb}$	15.3777	15.3710	15.2599	15.2840	15.2884	15.3060	15.2700	15.3031	15.3510	15.3541	15.3660
2σ	0.0002	0.0003	0.0003	0.0002	0.0003	0.0003	0.0002	0.0002	0.0002	0.0002	0.0003
$^{208}\text{Pb}/^{204}\text{Pb}$	37.9843	37.6764	37.3454	37.4561	37.5213	37.6082	37.4705	37.5883	37.5888	37.6524	37.9427
2σ	0.0011	0.0010	0.0010	0.0008	0.0009	0.0008	0.0008	0.0010	0.0009	0.0008	0.0009
$(^{206}\text{Pb}/^{204}\text{Pb})_{\text{t}}$	16.562	16.701	16.017	16.098	16.145	16.273	16.090	16.305	16.581	16.585	16.539
$(^{207}\text{Pb}/^{204}\text{Pb})_{\text{t}}$	15.347	15.368	15.252	15.269	15.274	15.292	15.265	15.295	15.349	15.349	15.347
$(^{208}\text{Pb}/^{204}\text{Pb})_{\text{t}}$	37.098	37.578	37.095	37.189	37.228	37.291	37.191	37.305	37.543	37.550	37.484

QEC003: rhyolite porphyry dike; QEC004, quartz porphyry dike; QEC005, QEC008, QEC010, QEC011, QEC012 and QEC014: biotite granite porphyry stocks; QEC018, QEC019 and QEC020: biotite granite porphyry dikes.

stock, the granite porphyry dike samples have slightly higher $^{87}\text{Rb}/^{86}\text{Sr}$ values (2.54–3.07), lower I_{Sr} values (0.70729 to 0.70768), higher $\epsilon\text{Nd}(t)$ values (−17.4 to −16.9), and lower $T_{\text{DM1}}(\text{Nd})$ (1.76–1.80 Ga) and $T_{\text{DM2}}(\text{Nd})$ (2.29–2.33 Ga). The $(^{206}\text{Pb}/^{204}\text{Pb})_t$, $(^{207}\text{Pb}/^{204}\text{Pb})_t$, and $(^{208}\text{Pb}/^{204}\text{Pb})_t$ values of the biotite granite porphyry stock and dike samples are 16.017–16.585, 15.252–15.349, and 37.095–37.550, respectively.

6. Discussion

6.1. Geochronology of the Qian'echong porphyry Mo deposit

Both the zircon U–Pb and the molybdenite Re–Os ages obtained in this study fall in a narrow time span of 130–122 Ma, which demonstrates that the Qian'echong porphyry Mo deposit was formed in the Early Cretaceous, as was previously suggested by M.Z. Yang et al. (2010). In addition, the zircon U–Pb ages of all studied porphyritic intrusions correspond fairly well to the individual molybdenite Re–Os ages, which suggest a causative relationship between the ores and the spatially associated plutonic rocks. Crystallization ages for molybdenite from the Qian'echong deposit range from 128.49 ± 1.40 to 123.31 ± 1.02 Ma, which is coeval with adjacent igneous rocks formed at 128.9 ± 1.1 to 124.7 ± 1.6 Ma.

The quartz porphyry dikes yield a zircon U–Pb age of ~129 Ma, which is essentially identical to the oldest molybdenite Re–Os age of ~128.5 Ma, indicating that the magmatic–hydrothermal system may have been initiated at that time. The rhyolite to granite porphyry dikes observed at the surface (127.42 ± 0.94 to 127.44 ± 0.98 Ma), the biotite granite porphyry dike at the depth (126.6 ± 1.4 Ma), and the buried biotite granite porphyry stock (124.7 ± 1.6 Ma) show similar composition in mineralogy and petrochemistry, and yield the same isotope ages within analytical error, suggesting that they might be formed at

different depths by the same magmatic system. Considering the analytical precision difference between LA-ICP-MS and SIMS, we here prefer to adopt the results obtained from SIMS, and to estimate the crystallization time of rhyolite and granite porphyry dikes and stock to be 126.5 ± 1.5 Ma. This granitic activity apparently formed much of the molybdenite mineralization defined at 126.23 ± 0.85 to 123.31 ± 1.02 Ma. The close association of the biotite granite porphyry stock with the main orebody (Fig. 3) indicates that emplacement of the biotite granite porphyry was the most important intrusive event in the formation of the Qian'echong Mo deposit.

A series of magmatic–hydrothermal pulses is common in giant mineral deposits. In the Dabie Shan, the other giant porphyry Mo deposit, Shapinggou, formed by at least two episodic magmatic events at 116 Ma and 113 Ma, respectively (H.J. Chen et al., 2013). In the Qinling Orogen, the giant Shangfanggou porphyry–skarn Mo–Fe system and Nannihu porphyry Mo–W system both resulted from multistage magmatism between 158 and 140 Ma (Yang et al., 2012; Y. Yang et al., 2013); and the Yuchiling porphyry Mo deposit in the Qinling was formed by three igneous events at ~143 Ma, ~138 Ma, and ~135 Ma, with corresponding molybdenite Re–Os ages of ~141 Ma, ~137 Ma, and ~134 Ma, respectively (N. Li et al., 2013). Ballard et al. (2001) distinguished two temporally distinct magmatic–hydrothermal pulses at 34.6 Ma and 33.5 Ma at the giant Chuquicamata Cu deposit in northern Chile, and considered the intensive quartz–sericite alteration developed at 31.1 Ma to have been caused by an additional concealed intrusion. Harris et al. (2008) revealed two episodes of porphyry intrusion at the Bajo de la Alumbrera porphyry Cu–Au deposit in Argentina, where the hydrothermal process appears to have lasted for at least 3 m.y. Using U–Pb, $^{40}\text{Ar}/^{39}\text{Ar}$, Re–Os, and fission track dating, Maksaeu et al. (2004) recognized five short-lived episodes of felsic intrusion-related mineralization at the El Teniente porphyry Cu–Mo deposit in Chile. In addition, the Antapaccay porphyry Cu–Au deposit, southern Peru (Jones et al.,

Table 6
Isotope ages of porphyry Mo systems in Dabie Shan.

Deposits	Porphyry/ores	N	Method	Age (Ma)	Reference
Qian'echong	Quartz porphyry dyke	1	SIMS zircon U–Pb weighted average	128.9 ± 1.1	This study
	Rhyolite porphyry	1	SIMS zircon U–Pb weighted average	127.4 ± 0.9	This study
	Outcropped granite porphyry dyke	1	SIMS zircon U–Pb weighted average	127.4 ± 1.3	This study
	Blinded granite porphyry dyke	1	SIMS zircon U–Pb weighted average	126.5 ± 1.3	This study
	Granite porphyry stock	1	LA-ICPMS zircon U–Pb weighted average	124.7 ± 1.6	This study
	Ores	6	Molybdenite Re–Os	123.31 ± 1.02 – 128.49 ± 1.40	This study
	Ores	6	Molybdenite Re–Os	127.9 ± 1.9 – 129.7 ± 1.9	Gao et al. (2014)
	Granite porphyry stock	2	SHRIMP zircon U–Pb weighted average	130 ± 2 , 129 ± 2	Gao et al. (2014)
	Outcropped granite porphyry dyke	1	LA-ICPMS zircon U–Pb weighted average	128.8 ± 2.6	M.Z. Yang et al. (2010)
	Ores	3	Molybdenite Re–Os	127.6 ± 1.8 – 128.0 ± 1.8	M.Z. Yang et al. (2010)
Shapinggou	Quartz syenite	2	LA-ICPMS zircon U–Pb weighted average	121.5 ± 1.3 – 122.51 ± 0.81	Meng et al. (2012)
	Syenite porphyry	1	LA-ICPMS zircon U–Pb weighted average	120.7 ± 1.1	Meng et al. (2012)
	Granite porphyry	1	LA-ICPMS zircon U–Pb concordia	111.5 ± 1.5	H. Zhang et al. (2011)
	Syenite porphyry	1	LA-ICPMS zircon U–Pb concordia	111.7 ± 1.9	H. Zhang et al. (2011)
	Quartz syenite porphyry	1	LA-ICPMS zircon U–Pb weighted average	116.1 ± 2.2	H.J. Chen et al. (2013)
	Magma matrix of breccias pipe	1	LA-ICPMS zircon U–Pb weighted average	112.9 ± 1.2	H.J. Chen et al. (2013)
	Wall-rock block of breccias pipe	1	LA-ICPMS zircon U–Pb weighted average	131.6 ± 2.6	H.J. Chen et al. (2013)
	Ores	7	Molybdenite Re–Os	110.18 ± 1.67 – 113.77 ± 3.65	H. Zhang et al. (2011)
	Ores	9	Molybdenite Re–Os	112.2 ± 1.7 – 113.9 ± 1.7	Huang et al. (2011)
	Ores	2	Molybdenite Re–Os	112.6 ± 1.3 – 113.5 ± 1.3	Xu et al. (2011)
	Ores	5	Molybdenite Re–Os	100.0 ± 1.8 – 113.6 ± 1.7	Meng et al. (2012)
Tangjiaping	Granite porphyry	1	LA-ICPMS zircon U–Pb concordia	121.6 ± 4.6	Wei et al. (2010)
	Ores	3	Molybdenite Re–Os weighted average	119.7 ± 2.1	Luo et al. (2010)
	Ores	5	Molybdenite Re–Os	113.5 ± 1.8 – 118.5 ± 1.9	Y. Li et al. (2013)
Dayinjian	Granite porphyry	1	LA-ICP-MS zircon U–Pb weighted average	124.9 ± 1.3	H.C. Li et al. (2012)
	Ores	7	Molybdenite Re–Os isochron	125.07 ± 0.87	H.C. Li et al. (2012)
	Ores	1	Molybdenite Re–Os	122.1 ± 2.4	Y. Li et al. (2013)
	Ores	4	Molybdenite Re–Os	121.5 ± 1.8 – 123.9 ± 2.0	Luo et al. (2010)
Tianmugou	Ores	1	Molybdenite Re–Os	121.6 ± 2.1	Y. Li et al. (2013)
	Ores	1	Molybdenite Re–Os	121.6 ± 2.1	Y. Li et al. (2013)
Mushan	Granite porphyry	1	LA-ICPMS zircon U–Pb weighted average	142.0 ± 1.8	Y. Li et al. (2013)
	Ores	1	Molybdenite Re–Os	155.7 ± 5.1	Y. Li et al. (2013)
Bao'anzhai	Granite porphyry	1	LA-ICPMS zircon U–Pb weighted average	135.3 ± 1.9	M.Z. Yang et al. (2010)
	Ore	1	Molybdenite Re–Os age	140.5 ± 8.2	Y. Li et al. (2013)

N: number of samples.

2007), and Los Pelambres porphyry Cu–Mo–Au deposit (Perelló et al., 2007) and the Escondida porphyry Cu deposit (Padilla-Garza et al., 2004) in Chile, have also been interpreted to have been formed by multiple magmatic–hydrothermal episodes. Therefore, the Mo mineralization at Qian'echong possibly resulted from two magmatic pulses, one at ~129 Ma and one at ~126.5 Ma.

6.2. The tectonic setting of the Qian'echong deposit

The Qinling–Dabie orogenic belt was formed during Late Triassic–Early Cretaceous and caused by collision of the Yangtze and North China blocks (Lin et al., 1985; Yuan et al., 2003; Li et al., 2007, 2011, 2015), as supported by the formation of the ultrahigh-pressure eclogites in the Dabie Shan (Ames et al., 1993; Chavagnac and Jahn, 1996). Paleomagnetic studies have shown that the convergence between the blocks had ended by the Late Jurassic (Lin et al., 1985; Zhu et al., 1998). The subsequent Early Cretaceous geodynamic setting in the Qinling–Dabie belt was one of post-collisional extension (Jahn et al., 1999; Chen et al., 2007, 2009), as the influence of plate motions in the Pacific basin became significant (Mao et al., 2011). Our new zircon U–Pb and molybdenite Re–Os dates confirm that the Mo mineralization and its causative magmatism at the Qian'echong deposit were products of the post-collision tectonic setting.

In the Dabie Shan, the ages of Mo deposits and their associated intrusions range between 142 Ma and 110 Ma (Table 6). This time span is quite similar to that established for the Mo deposits in the eastern Qinling (Chen et al., 2000; Li et al., 2007; Mao et al., 2010; N. Li et al., 2012a, 2013; and references therein). Both groups of large mid-Yanshanian deposits are specifically related to the post-collisional regime (Chen and Fu, 1992; Chen et al., 2000; Mao et al., 2011; Y. Li et al., 2013). In the (Y + Nb)–Rb and Rb/30–Hf–Ta*3 tectonic discrimination diagrams (Fig. 11), the porphyry dikes and stocks plot primarily in the post-collisional granite domain, consistent with magma that originated from partial melting of the continental crust in a post-collisional setting.

6.3. The origin of the intrusions at Qian'echong deposit

The Sr–Nd–Pb isotopic compositions of the Early Cretaceous granitoids in the Dabie Shan are generally similar to those of the northern Dabie complex (NDC), but different from those of the southern Dabie complex (SDC) (Figs. 12 and 13). Consequently, the origins of the Early Cretaceous granitoids have been widely debated with three main views: (1) the granitoids were formed by partial melting of the

gneisses and amphibolites from the NDC (Zhang et al., 2002); (2) they were derived from a mixture of the NDC and the basement of the Yangtze block, likely represented by the Kongling Group gneisses in western Hubei province, because the zircon $T_{DM2}(Hf)$ values of the granitoids are older than those of the NDC (Zhao et al., 2008, 2011; Gao et al., 2014); or (3) they originated from the partial melting of the NDC and the southward underthrusting of allochthons from the North China block (H.J. Chen et al., 2013), because the isotopic signatures of both the Early Cretaceous granitoids and andesitic to mafic rocks in the Dabie Shan are similar to those of the subcontinental lithospheric mantle of the North China block (Jahn et al., 1999; Ma et al., 2000; Jahn and Chen, 2007; Xu et al., 2012). Several geologists (e.g., Chen et al., 2005; N. Li et al., 2012a) also suggested that the contribution of the subcontinental lithospheric mantle to the Cretaceous magmatism increased with time, with an associated post-collisional lithospheric extension and thinning.

In Fig. 12A and B, the samples from the Qian'echong porphyry system completely scatter within the domains defined for the NDC and the Precambrian rocks of the North China block, which is a feature shared also by the Early Cretaceous granitoids and mafic to andesitic rocks in Dabie Shan. On the contrary, their $^{207}Pb/^{204}Pb$, $^{206}Pb/^{204}Pb$ and $^{208}Pb/^{204}Pb$ ratios are far lower than those of the SDC and Tongling granite (Fig. 12). The Tongling granite, located along the northern margin of the Yangtze block, is typical of Mesozoic igneous rocks that originated from the partial melting of the Yangtze block crust (Zhang, 1995). Thus it is unlikely that the Qian'echong porphyry system has a genetic relationship to either the Yangtze Craton or the SDC. Moreover, the intrusive rocks at Qian'echong deposit show a decrease in Pb isotope ratios with a decrease in age, with the values of the quartz porphyry dike being the highest and shifting to the domain of the SDC (Fig. 12).

It is important to note, however, that the quartz porphyry dike yields the oldest age (>128 Ma) and the uniquely highest I_{Sr} value for the intrusive rocks in the Qian'echong area, and shows Sr–Nd isotope signatures consistent with derivation from the SDC (Fig. 13). This implies that the quartz porphyry dike must be mainly sourced from the SDC (Fig. 14A), and not the NDC and/or the basement of the North China block. The other intrusive rocks are all younger than 128 Ma and show slightly lower $\epsilon Nd(t)$ and I_{Sr} values than the NDC, but completely fall in the domain of the contemporaneous granitoids in the Dabie Shan (Figs. 12 and 13; Zhang et al., 2002; Jahn and Chen, 2007; He et al., 2013). These rocks partly overlap the field of the NDC (Fig. 13), and particularly rocks of the Taihua and Xiong'er Groups that are the main lithologies along the southern margin of the North China block (Deng

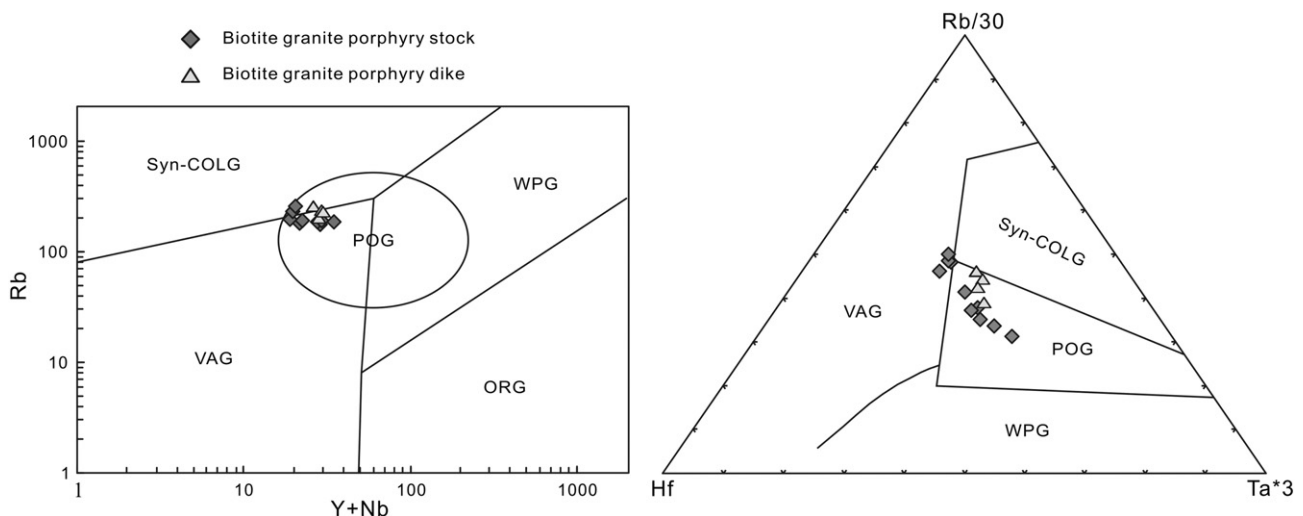


Fig. 11. The (Y + Nb)–Rb (Pearce, 1996) and Rb/30–Hf–3Ta (Harris et al., 1986) tectonic discrimination diagrams for the biotite granite porphyry dike and stock at the porphyry Mo Qian'echong deposit. VAG, volcanic arc granites; ORG, oceanic ridge granites; WPG, within-plate granites; Syn-COLG, syn-collision granites; POG, post-collision granites.

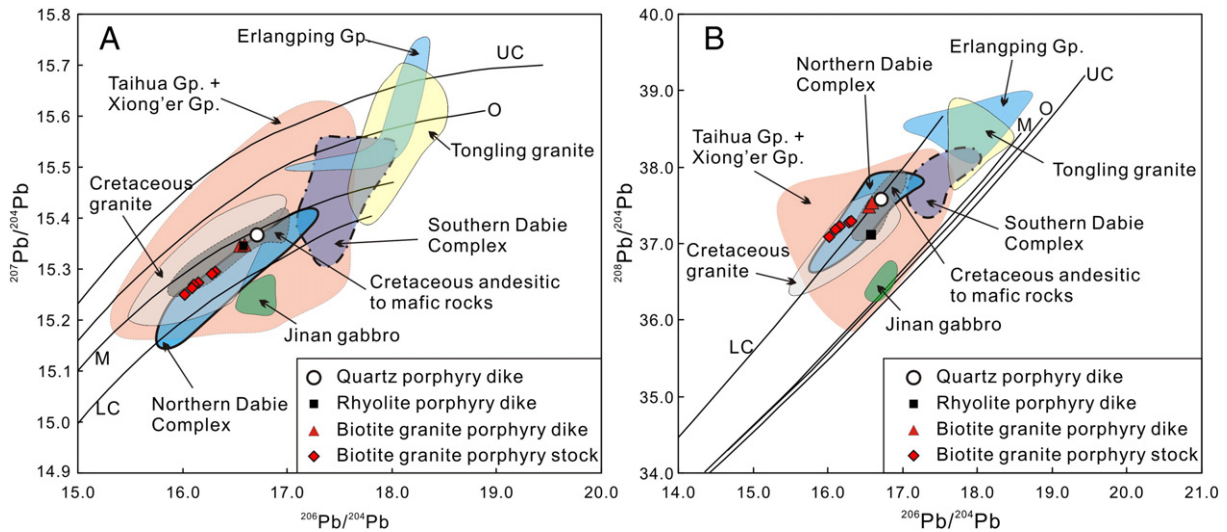


Fig. 12. Correlative diagrams of $^{207}\text{Pb}/^{204}\text{Pb}$ vs. $^{206}\text{Pb}/^{204}\text{Pb}$ (A) and $^{208}\text{Pb}/^{204}\text{Pb}$ vs. $^{206}\text{Pb}/^{204}\text{Pb}$ (B) for intrusions at the Qian'echong porphyry Mo deposit (calculated back to $t = 125$ Ma). Data also include: the gneisses and amphibolites of the Northern Dabie Complex (Zhang et al., 2002); gneisses and eclogites of the Southern Dabie Complex (Zhang et al., 2002); Early Cretaceous granitoids (Zhang et al., 2002) and intermediate–ultramafic rocks (Jahn et al., 1999; Chen et al., 2002) in the Dabie Shan; Tongling granite at the joint of the Yangtze Craton and Dabie Shan, Anhui Province (Zhang, 1995); Erlangping Group (J. Zhang et al., 2011), Xiong'er Group (Deng et al., 2013c), and Taihua Group (Ni et al., 2012); and Jinan gabbro (Zhang et al., 2004). All the data are calculated back to 125 Ma, except for the Xiong'er and Taihua Groups. Base map is cited from Zartman and Doe (1981).

et al., 2013a,b,c). They are suggested to have originated from a source dominated by NDC that mixed with the Precambrian rocks of the North China block (Fig. 14A). This interpretation is supported by seismic reflectance data (e.g., Yuan et al., 2003), and by the $T_{\text{DM}2}(\text{Nd})$ values of the Qian'echong porphyries that range from 2.24 to 3.03 Ga, which is consistent with the ages of Taihua Group (<2.26–2.84 Ga; Xu et al., 2009).

To interpret the origin of the Qian'echong porphyry system, we present a tectonic model that shows a northward subduction of the Yangtze block before 128 Ma (Fig. 14A), followed by a northward, vertical

tectonic extrusion of the Dabie Shan onto the basement of the North China block after 128 Ma (Fig. 14A). This tectonic reversal at ~128 Ma was possibly related to the delamination of the lithosphere root of the Dabie Shan (Ma et al., 2000; Pirajno, 2013), which caused the exhumation of UHP rocks (Jahn et al., 1999; Zheng et al., 2006), the generation of voluminous magmas (Chen et al., 2002; Zhao et al., 2011), and the development of hydrothermal mineral systems (e.g., Y. Li et al., 2013; Goldfarb and Santosh, 2014). Formation of the Qian'echong Mo deposit is also shown to be a consequence of this tectonic reversal (Fig. 14B).

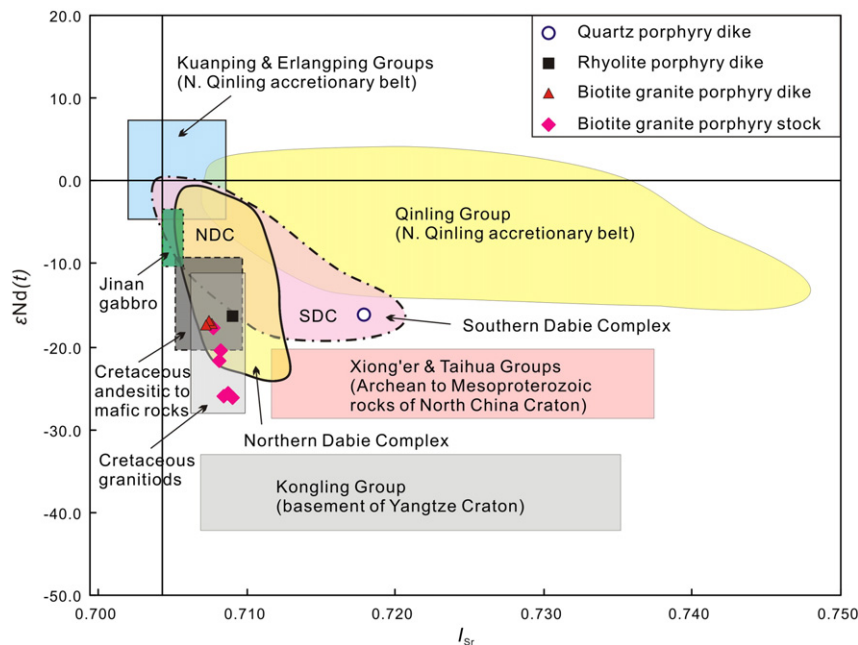


Fig. 13. Correlative diagram of $\epsilon\text{Nd}(t)$ vs. I_{Sr} for intrusions at the Qian'echong porphyry Mo deposit. For comparison, the Sr–Nd isotopic compositions are also plotted for the gneisses and amphibolites from the Northern Dabie Complex (NDC; Ma et al., 2000), gneisses and eclogites from the Southern Dabie Complex (SDC; Xia et al., 2008), Early Cretaceous granitoids (Zhang et al., 2002; Zhao et al., 2011; He et al., 2013) and intermediate–ultramafic rocks (Jahn et al., 1999; Zhao et al., 2011; Xu et al., 2012) in the Dabie Shan, Kongling Group (K. Chen et al., 2013), Xiong'er Group (He et al., 2010; Deng et al., 2013c), Taihua Group (Xu et al., 2009; Ni et al., 2012), Qinling Group (Zhang et al., 1994), Kuanping Group (Zhang et al., 1994; Liu et al., 2013), Erlangping Group (Liu et al., 2013), and Jinan gabbro (Zhang et al., 2004), calculated back to $t = 125$ Ma.

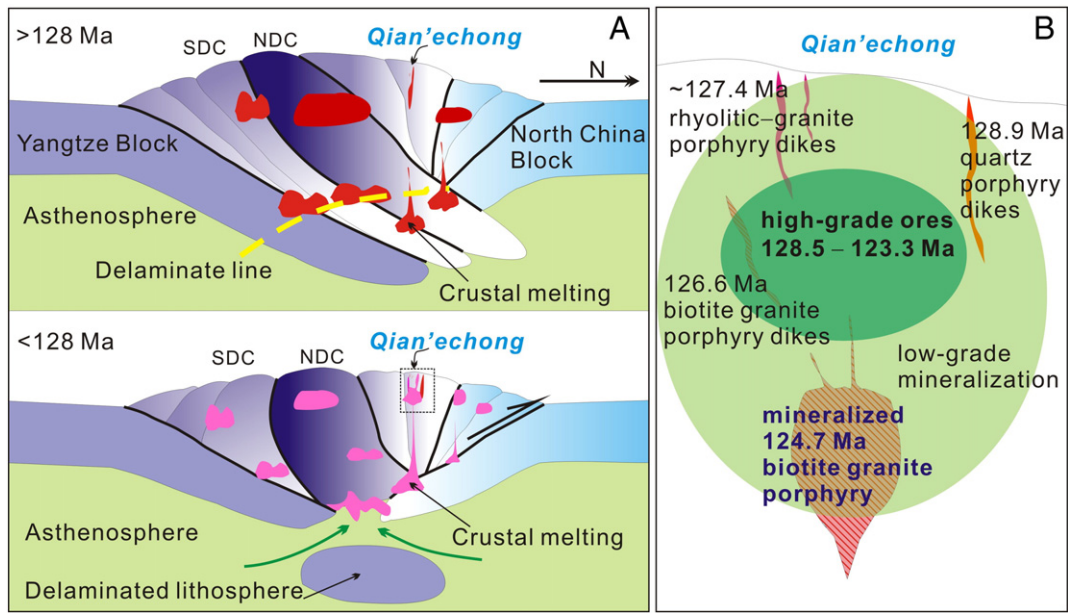


Fig. 14. Conceptual models that show the tectonic setting of the Qian'echong porphyry Mo system (A; modified after Yuan et al., 2003) and the spatial relationship between orebodies and porphyry stock and dikes (B).

6.4. A new type of porphyry Mo deposit: collisional-type?

The orebodies in porphyry deposits are traditionally considered to occur in the causative porphyry stocks that generally originated from subduction of an oceanic slab, slab melts interacting with overlying mantle, enriched subcontinental lithospheric mantle, and crust, and mixing of magmas derived from these various source areas (e.g. Sillitoe, 1972; Richards, 2003; Pirajno, 2009; Richards, 2009, 2011; Pirajno, 2013). The porphyry deposits mainly occur in magmatic arcs, with a small number developing in other settings (e.g. Richards et al., 1990; Chen et al., 2000; Richards, 2003; Chen et al., 2007; Chen and Li, 2009; Richards, 2009). Compared to the majority of the porphyry deposits, the giant Qian'echong porphyry Mo system is unique because of its crustal source for Mo and the location of the orebodies in the country rocks to the main intrusions (out-porphyry; Figs. 3 and 14B). These features lead us to define the Qian'echong deposit as representative of a new type of porphyry Mo deposit.

Previous studies have classified porphyry Mo deposits into two types (Carten et al., 1993; Selby et al., 2000). One commonly develops in subduction-related continental arcs, is associated with relatively less differentiated calc-alkaline magmas, and is characterized by low F contents and low Mo-grades, such as those that are represented by the Endako (Selby et al., 2000) and MAX deposits (Linnen and Williams-Jones, 1990; Lawley et al., 2010) in British Columbia, Canada (e.g., magmatic arc-, subduction- or Endako-type). The other is formed in rift-related back-arc settings, is associated with highly evolved, silicic-alkalic magmas, and is characterized by high F contents and high Mo-grades, as exemplified by Climax (Wallace, 1995), Urad-Henderson (Seedorff and Einaudi, 2004a,b) and Questa (Klemm et al., 2008) in the Rocky Mountain province, USA (e.g., rift- or Climax-type). According to Selby et al. (2000), in the magmatic arc-type Mo deposits, low- to moderate-salinity (1–10 wt.% NaCl equiv.), liquid-rich and vapor-rich aqueous inclusions and aqueous-carbonic inclusions coexist with less abundant saline (30–60 wt.% NaCl equiv.) inclusions; by

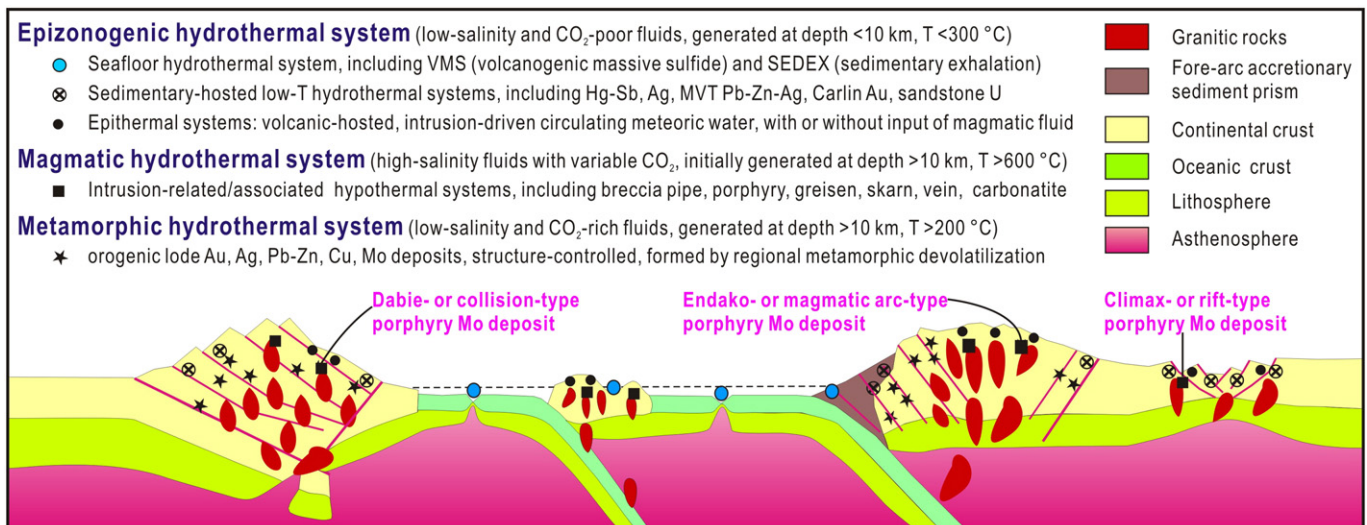


Fig. 15. Global tectonic settings for three types of porphyry Mo deposits. Compiled after Goldfarb et al. (2001) and Chen (2013).

contrast, in rift-type deposits, there are abundant coexisting saline (30–65 wt.% NaCl equiv.) and vapor-rich aqueous inclusions, and coexisting low- to moderate-salinity aqueous inclusions (1–20 wt.% NaCl equiv.) and aqueous-carbonic inclusions (Fig. 15).

The Qian'echong Mo deposit does not fit into either of these two types of Mo porphyry deposits. The high contents of alkalis and incompatible elements (Table 1) and strong fluoritization suggest an affinity with rift- or Climax-type deposits, but the much lower Mo grade, the crustal magmatic source, and the external occurrence of orebodies are distinct from the rift-type deposits. The deposit is located in a collision orogen, and was formed in a post-collisional time, which is inconsistent with rifts or magmatic arcs. In addition to the aqueous-carbonic and halite-bearing fluid inclusions that typically occur in both types of porphyry Mo deposits, the Qian'echong deposit is unique due to its carbonic inclusions, its multiple daughter mineral-bearing aqueous-carbonic inclusions, and its absence of halite daughter minerals (Y.F. Yang et al., 2013). Unlike the rift- and magmatic arc-type deposits, where phyllic and propylitic alteration assemblages are well developed (Ludington and Plumlee, 2009), the hydrothermal alteration at the Qian'echong deposits is predominantly potassic, with less extensive silicification, phyllic assemblages and propylitic assemblages, as well as some carbonatization and fluoritization (Y.F. Yang et al., 2013). It is noteworthy that the abovementioned characteristics of the Qian'echong deposit are widely shared by other porphyry Mo deposits located in post-collisional settings, such as at Yaochong (Wang et al., 2014) in the Dabie Shan; Donggou (Y.F. Yang et al., 2011), Yuchiling (N. Li et al., 2012b), Nannihu (Yang et al., 2012), Shangfanggou (Y. Yang et al., 2013), and Jinduicheng (Yang et al., 2009) in the eastern Qinling; Donggebi (Wu et al., 2013) and Baishan (Xiang et al., 2013) in the eastern Tian Shan; and many porphyry Mo deposits in the northeastern China (Chen et al., 2012). Hence, we assign these deposits to a new type of porphyry Mo deposit, termed collisional- or Dabie-type, exemplified by the Qian'echong deposit, with a new genetic model showing generation in a collisional tectonic setting, rather than in rift (Climax) or magmatic arc (Endako) environments.

7. Concluding remarks

All the granitic rocks at the Qian'echong deposit have relatively high SiO₂, K₂O, and Al₂O₃, and low TiO₂, MgO, and CaO. They have high LREE contents and negative Eu anomalies, and show high-K calc-alkaline to shoshonite affinity, suggesting that they were mainly originated from the melting of continental crust.

Zircon grains from quartz porphyry dyke, rhyolitic to granite porphyry dikes, and granite porphyry stock, yield U–Pb isotope ages of 128.9 ± 1.1 Ma, 127.44 ± 0.98 to 126.6 ± 1.4 Ma, and 124.7 ± 1.6 Ma, respectively. These ages are correlative with molybdenite crystallization ages measured at 128.5 Ma, 126.2–125 Ma, and 124–123 Ma. The giant Qian'echong porphyry Mo deposit was formed by a multistage magmatic–hydrothermal process from about 129 to 123 Ma.

The Sr–Nd–Pb isotope signatures of the granitic rocks indicate that the >128 Ma quartz porphyry dike was formed by northwardly subducted rocks of the southern Dabie complex, whereas the other porphyry dikes and stock with ages of <128 Ma were mainly sourced from both basement rocks of the North China block and the northern Dabie complex. Hence, since ca 128 Ma, the basement of North China block was overridden by the northern Dabie complex, which possibly resulted from vertical, northward tectonic extrusion of the Dabie Shan that was associated with delamination of its lithospheric root.

The Qian'echong Mo deposit was formed by two pulses of a short-lived magmatic–hydrothermal event, coeval with other middle Yanshanian (160–100 Ma) Mo deposits in the Qinling Orogen and Dabie Shan. Compared with the Climax- and Endako-type Mo deposits, it is unique because of the crustal source of the causative porphyry, mineralization mainly outside of the porphyry, the CO₂-, K-, and F-rich ore-forming fluids, and a post-collisional tectonic setting, and thus is

proposed to represent a new type of porphyry Mo deposit, termed collisional- or Dabie-type.

Acknowledgments

The research was supported by a grant from the Excellent Ph.D. Thesis Program of Beijing (no. 20131000104), the National 973-Program (Projects 2012CB406602 and 2006CB403508), and NSFC (nos. 41203029 and 40730421). The field investigation was supported by Geological Team 3 of the Henan Bureau of Land and Resources. Relevant comments, careful corrections, and constructive suggestions from the reviewers and Professor Richard Goldfarb greatly improved the quality of the manuscript.

References

- Ames, L., Tilton, G.R., Zhou, G., 1993. Timing of collision of the Sino-Korean and Yangtze Cratons: U–Pb zircon dating of coesite-bearing eclogites. *Geology* 21, 239–342.
- Anderson, T., 2002. Correction of common lead in U–Pb analyses that do not report ²⁰⁴Pb. *Chemical Geology* 192, 59–79.
- Ballard, J.R., Palin, J.M., Williams, L.S., Campbell, I.H., Faunes, A., 2001. Two ages of porphyry intrusion resolved for the super-giant Chuquibambilla copper deposit of northern Chile by ELA-ICP-MS and SHRIMP. *Geology* 29, 383–386.
- Black, L.P., Kamo, S.L., Allen, C.M., Aleinikoff, J.N., Davis, D.W., Korsch, R.J., Foudoulis, C., 2003. TEMORA 1: a new zircon standard for Phanerozoic U–Pb geochronology. *Chemical Geology* 200, 155–170.
- Carten, R.B., White, W.H., Stein, H.J., 1993. High-grade granite-related molybdenum systems: classification and origin. *Geological Association of Canada Special Paper* 40, 521–554.
- Chavagnac, V., Jahn, B.M., 1996. Coesite-bearing eclogites from the Bixiling Complex, Dabie Mountains, China: Sm–Nd ages, geochemical characteristics and tectonic implications. *Chemical Geology* 133, 29–51.
- Chen, Y.J., 2013. The development of continental collision metallogeny and its application. *Acta Petrologica Sinica* 29, 1–17 (in Chinese with English abstract).
- Chen, Y.J., Fu, S.G., 1992. Gold Mineralization in West Henan, China. *Seismological Press, Beijing*, p. 234 (in Chinese with English abstract).
- Chen, Y.J., Li, N., 2009. Diagnostic fluid inclusion and wallrock alteration of intrusion-related hypothermal ore-systems (porphyry, skarn, breccia pipe, vein and IOCG) formed in intracontinental settings: origin and difference from those in volcanic arc. *Acta Petrologica Sinica* 25, 2477–2508 (in Chinese with English abstract).
- Chen, Y.J., Wang, Y., 2011. Fluid inclusion study of the Tangjiaping Mo deposit, Dabie Shan, Henan Province: implications for the nature of porphyry systems of post-collisional tectonic settings. *International Geology Review* 53, 635–655.
- Chen, Y.J., Li, C., Zhang, J., Li, Z., Wang, H.H., 2000. Sr and O isotopic characteristics of porphyries in the Qinling molybdenum deposit belt and their implication to genetic mechanism and type. *Science in China Series D* 43 (Suppl.), 82–94.
- Chen, B., Jahn, B.M., Wei, C.J., 2002. Petrogenesis of Mesozoic granitoids in the Dabie UHP complex, central China: trace element and Nd–Sr isotope evidence. *Lithos* 60, 67–88.
- Chen, Y.J., Pirajno, F., Qi, J.P., 2005. Origin of gold metallogeny and sources of ore-forming fluids, in the Jiaodong province, eastern China. *International Geology Review* 47, 530–549.
- Chen, Y.J., Chen, H.Y., Zaw, K., Pirajno, F., Zhang, Z.J., 2007. Geodynamic settings and tectonic model of skarn gold deposits in China: an overview. *Ore Geology Reviews* 31, 139–169.
- Chen, Y.J., Zhai, M.G., Jiang, S.Y., 2009. Significant achievements and open issues in study of orogenesis and metallogenesis surrounding the North China continent. *Acta Petrologica Sinica* 25, 2695–2726 (in Chinese with English abstract).
- Chen, Y.J., Zhang, C., Li, N., Yang, Y.F., Deng, K., 2012. Geology of the Mo deposits in Northeast China. *Journal of Jilin University (Earth Science)* 42, 1223–1268 (in Chinese with English abstract).
- Chen, H.J., Chen, Y.J., Zhang, J., Chen, X.Z., Zhang, H.D., 2013a. Zircon U–Pb ages and Hf isotope characteristics of the ore-bearing intrusion from the Shapingou molybdenum deposit, Jinzhai County, Anhui Province. *Acta Petrologica Sinica* 29, 131–145 (in Chinese with English abstract).
- Chen, K., Gao, S., Wu, Y.B., Guo, J.L., Hu, Z.C., Liu, Y.S., Zong, K.Q., Liang, Z.W., Geng, X.L., 2013b. 2.6–2.7 Ga crustal growth in Yangtze Craton, South China. *Precambrian Research* 224, 472–490.
- Chernyshev, I.V., Chugaev, A.V., Shatagin, K.N., 2007. High-precision Pb isotope analysis by multicollector-ICP-mass-spectrometry using ²⁰⁵Tl/²⁰³Tl normalization: optimization and calibration of the method for the studies of Pb isotope variations. *Geochemistry International* 45, 1065–1076.
- Deng, X.H., Chen, Y.J., Santosh, M., Yao, J.M., 2013a. Genesis of the 1.76 Ga Zhaiwa Mo–Cu and its link with the Xiong'er volcanics in the North China Craton: implications for accretionary growth along the margin of the Columbia supercontinent. *Precambrian Research* 227, 337–348.
- Deng, X.H., Chen, Y.J., Santosh, M., Yao, J.M., 2013b. Re–Os geochronology, fluid inclusions and genesis of the 0.85 Ga Tumen molybdenite–fluorite deposit in Eastern Qinling, China: implications for pre-Mesozoic Mo–enrichment and tectonic setting. *Geological Journal*. <http://dx.doi.org/10.1002/gj.2520>.
- Deng, X.H., Chen, Y.J., Santosh, M., Zhao, G.C., Yao, J.M., 2013c. Metallogeny during continental outgrowth in the Columbia supercontinent: isotopic characterization of the Zhaiwa Mo–Cu system in the North China Craton. *Ore Geology Reviews* 51, 43–56.

- DePaolo, D.J., Wasserburg, G.J., 1979. Petrogenetic mixing models and Nd–Sr isotopic patterns. *Geochimica et Cosmochimica Acta* 43, 615–627.
- Gao, Y., Mao, J.W., Ye, H.S., Li, F.L., Li, Y.F., Luo, Z.Z., Xiong, B.K., Meng, F., 2014. Geochronology, geochemistry and Sr–Nd–Pb isotopic constraints on the origin of the Qian'echong porphyry Mo deposit, Dabie orogen, east China. *Journal of Asian Earth Sciences* 85, 163–177.
- Geological Survey Team 3 of Henan Bureau of Land and Resources, 2009. Exploration Report of the Qian'echong Mo deposit, Guangshan County, Henan Province, (in Chinese).
- Goldfarb, R.J., Santosh, M., 2014. The dilemma of the Jiaodong gold deposits: are they unique? *Geoscience Frontiers* 4, 139–153.
- Goldfarb, R.J., Groves, D.I., Gardoll, S., 2001. Orogenic gold and geologic time: a global synthesis. *Ore Geology Reviews* 18, 1–75.
- Hacker, B.R., Ratschbacher, L., Webb, L., 2000. Exhumation of ultrahigh-pressure continental crust in east central China: late Triassic–early Jurassic tectonic unroofing. *Journal of Geophysical Research* 105 (B6), 13339–13364.
- Harris, N.B.W., Pearce, J.A., Tindle, A.G., 1986. Geochemical characteristics of collision-zone magmatism. In: Coward, M.P., Ries, A.C. (Eds.), *Collision Tectonics*. Geological Society Special Publication No. 19. Blackwell, pp. 67–81.
- Harris, A.C., Dunlap, W.J., Reiners, P.W., Allen, C.M., Cooke, D.R., White, N.C., Campbell, I.H., Golding, S.D., 2008. Multimillion year thermal history of a porphyry copper deposit: application of U–Pb, $^{40}\text{Ar}/^{39}\text{Ar}$ and (U–Th)/He chronometers, Bajo de la Alumbrera copper–gold deposit, Argentina. *Mineralium Deposita* 43, 295–314.
- He, Y.H., Zhao, G.C., Sun, M., Han, Y.G., 2010. Petrogenesis and tectonic setting of volcanic rocks in the Xiaoshan and Waifangshan areas along the southern margin of the North China Craton: constraints from bulk-rock geochemistry and Sr–Nd isotopic composition. *Lithos* 114, 186–199.
- He, Y.S., Li, S.G., Hoefs, J., Kleinhanns, I.C., 2013. Sr–Nd–Pb isotopic compositions of Early Cretaceous granitoids from the Dabie orogeny: constraints on the recycled lower continental crust. *Lithos* 156–159, 204–217.
- Henan Bureau of Geology and Mineral Resources, 1989. *The Regional Geology of Henan Province*. Geological Publishing House, Beijing, p. 772 (in Chinese).
- Huang, F., Wang, D.H., Lu, S.M., Chen, Y.C., Wang, B.H., Li, C., 2011. Molybdenite Re–Os isotopic age of Shapinggou Mo deposit in Anhui Province and Mesozoic Mo ore-forming stages in East Qinling–Dabie Mountains. *Mineral Deposits* 30, 1039–1057 (in Chinese with English abstract).
- Jacobsen, S.B., Wasserburg, G.J., 1980. Sm–Nd isotopic evolution of chondrites. *Earth and Planetary Science Letters* 50, 139–155.
- Jahn, B.M., Chen, B., 2007. Dabieshan UHP metamorphic terrane: Sr–Nd–Pb isotopic constraint to pre-metamorphic subduction polarity. *International Geology Review* 49, 14–29.
- Jahn, B.M., Wu, F.Y., Lo, C.H., Tsai, C.H., 1999. Crust–mantle interaction induced by deep subduction of the continental crust: geochemical and Sr–Nd isotopic evidence from post-collisional mafic–ultramafic intrusions of the northern Dabie complex, central China. *Chemical Geology* 157, 119–146.
- Jones, B., Kamenetsky, V., Davidson, P., Allen, C., 2007. Antapaccay porphyry Cu–Au deposit: a product of Andean tectonism and evolving magmatism, late Eocene–early Oligocene Abancay batholith, Altiplano, southern Peru: ores and orogenesis. Abstracts of Symposium Honoring the Career of William R. Dickinson. Arizona Geological Society, Tucson, pp. 132–133.
- Klemm, L.M., Pettke, T., Heinrich, C.A., 2008. Fluid and source magma evolution of the Questa porphyry Mo deposit, New Mexico, USA. *Mineralium Deposita* 43, 533–552.
- Lawley, C.J.W., Richard, J.P., Anderson, R.G., Creaser, R.A., Heaman, L.M., 2010. Geochronology and geochemistry of the MAX porphyry Mo deposit and its relationship to Pb–Zn–Ag mineralization, Kootenay Arc, Southern British Columbia, Canada. *Economic Geology* 105, 1113–1142.
- Lee, C.Y., Tsai, J.H., Ho, H.H., Yang, T.F., Chung, S.L., Chen, C.H., 1997. Quantitative analysis in rock samples by an X-ray fluorescence spectrometer, (I) major elements. Annual Meeting of the Geological Society of China, Program with Abstract, pp. 418–420 (in Chinese).
- Li, X.H., 1997. Geochemistry of the Longsheng Ophiolite from the southern margin of Yangtze Craton, SE China. *Geochemical Journal* 31, 323–337.
- Li, N., Chen, Y.J., Zhang, H., Zhao, T.P., Deng, X.H., Wang, Y., Ni, Z.Y., 2007. Molybdenum deposits in East Qinling. *Earth Science Frontiers* 14, 186–198 (in Chinese with English abstract).
- Li, X.H., Liu, Y., Li, Q.L., Guo, C.H., Chamberlain, K.R., 2009. Precise determination of Phanerozoic zircon Pb/Pb age by multicollector SIMS without external standardization. *Geochemistry, Geophysics, Geosystems* 10, Q04010. <http://dx.doi.org/10.1029/2009GC002400>.
- Li, Q.L., Li, X.H., Liu, Y., Tang, G.Q., Yang, J.H., Zhu, W.G., 2010. Precise U–Pb and Pb–Pb dating of Phanerozoic baddeleyite by SIMS with oxygen flooding technique. *Journal of Analytical Atomic Spectrometry* 25, 1107–1113.
- Li, N., Chen, Y.J., Fletcher, I.R., Zeng, Q.T., 2011. Triassic mineralization with Cretaceous overprint in the Dahu Au–Mo deposit, Xiaqingling gold province: constraints from SHRIMP monazite U–Th–Pb geochronology. *Gondwana Research* 20, 543–552.
- Li, H.C., Xu, Z.W., Lu, X.C., Chen, W., Qu, W.J., Fu, B., Yang, X.N., Yang, J., Chen, J.Q., 2012a. Constraints on timing and origin of the Dayinjian intrusion and associated molybdenum mineralization, western Dabie orogen, central China. *International Geology Reviews* 54, 1579–1596.
- Li, N., Chen, Y.J., Pirajno, F., Gong, H.J., Mao, S.D., Ni, Z.Y., 2012b. LA–ICP–MS zircon U–Pb dating, trace element and Hf isotope geochemistry of the Heyu granite batholith, eastern Qinling, central China: implications for Mesozoic tectono-magmatic evolution. *Lithos* 142–143, 34–47.
- Li, N., Ulrich, T., Chen, Y.J., Thompson, T.B., Peace, V., Pirajno, F., 2012c. Fluid evolution of the Yuchiling porphyry Mo deposit, East Qinling, China. *Ore Geology Reviews* 48, 442–459.
- Li, N., Chen, Y.J., Pirajno, F., Ni, Z.Y., Sun, Y.L., 2013a. Timing of the Yuchiling giant porphyry Mo system, eastern Qinling, central China, and implications for ore genesis. *Mineralium Deposita* 48, 505–524.
- Li, Y., Li, N., Yang, Y.F., Wang, P., Mi, M., Zhang, J., Chen, H.J., Chen, Y.J., 2013b. Geological features and geodynamic settings of the Mo deposits in the north segment of the Dabie Mountains. *Acta Petrologica Sinica* 29, 95–106 (in Chinese with English abstract).
- Li, N., Chen, Y.J., Santosh, M., Pirajno, F., 2014. Compositional polarity of Triassic granitoids in the Qinling Orogen, China: implication for termination of the northernmost paleo-Tethys. *Gondwana Research* 27, 244–257.
- Lin, J.L., Fuller, M., Zhang, W.Y., 1985. Preliminary Phanerozoic polar wander paths for the North and South China Blocks. *Nature* 313, 444–449.
- Linnen, R.L., Williams-Jones, A.E., 1990. Evolution of aqueous-carbonic fluids during contact metamorphism, wall-rock alteration, and molybdenite deposition at Trout Lake, British Columbia. *Economic Geology* 85, 1840–1856.
- Liu, F.L., Liou, J.G., 2011. Zircon as the best mineral for P–T–time history of UHP metamorphism: a review on mineral inclusions and U–Pb SHRIMP ages of zircons from the Dabie–Sulu UHP rocks. *Journal of Asian Earth Sciences* 40, 1–39.
- Liu, X.C., Jahn, B.M., Liu, D.Y., Dong, S.W., Li, S.Z., 2004. SHRIMP U–Pb zircon dating of a metagabbro and eclogites from western Dabieshan (Hong'an Block), China, and its tectonic implications. *Tectonophysics* 394, 171–192.
- Liu, X.C., Jahn, B.M., Dong, S.W., Lou, Y.X., Cui, J.J., 2008a. High-pressure metamorphic rocks from Tongbaishan, central China: U–Pb and $^{40}\text{Ar}/^{39}\text{Ar}$ age constraints on the provenance of protoliths and timing of metamorphism. *Lithos* 105, 301–318.
- Liu, Y.S., Hu, Z.C., Gao, S., Gunther, D., Xu, J., Gao, C.G., Chen, H.H., 2008b. In situ analysis of major and trace elements of anhydrous minerals by LA–ICP–MS without applying an internal standard. *Chemical Geology* 257, 34–43.
- Liu, X.C., Jahn, B.M., Li, S.Z., Liu, Y.S., 2013. U–Pb zircon age and geochemical constraints on tectonic evolution of Paleozoic accretionary orogenic system in the Tongbai orogen, central China. *Tectonophysics* 599, 67–88.
- Ludington, S., Plumlee, G.S., 2009. Climax-type porphyry molybdenum deposits. U.S. Geological Survey open file report 2009–1215, p. 16.
- Ludwig, K.R., 2003. User's Manual for Isoplot 3.0: a geochronological toolkit for Microsoft Excel. Berkeley Geochron Center Special publication 4, 1–71.
- Lugmair, G.W., Marti, K., 1978. Lunar initial $^{143}\text{Nd}/^{144}\text{Nd}$: differential evolution of the lunar crust and mantle. *Earth and Planetary Science Letters* 39, 349–357.
- Luo, Z.Z., Li, Y.F., Wang, Y.T., Wang, X.G., 2010. The molybdenite Re–Os age of Dayinjian molybdenum deposit in the northern margin of the Dabie Mountain, Xinxian area, Henan, China and its significance. *Geological Bulletin of China* 29, 1349–1354 (in Chinese with English abstract).
- Ma, C.Q., Ehlers, C., Xu, C.H., Li, Z.C., Yang, K.G., 2000. The roots of the Dabieshan ultrahigh-pressure metamorphic terrane: constraints from geochemistry and Nd–Sr isotope systematics. *Precambrian Research* 102, 279–301.
- Maksaeve, V., Munizaga, F., McWilliams, M., Fanning, M., Mathur, R., Ruiz, J., Zentelli, M., 2004. New chronology for El Teniente, Chilean Andes, from U–Pb, $^{40}\text{Ar}/^{39}\text{Ar}$, Re–Os and fission track dating. In: Sillitoe, R.H., Perello, J., Vidal, C.E. (Eds.), *Andean Metallogeny: New Discoveries. Concepts and Updates*. Society of Economic Geologists Special Publication, Boulder, pp. 15–54.
- Mao, J.W., Xie, G.Q., Bierlein, F., Qü, W.J., Du, A.D., Ye, H.S., Pirajno, F., Li, H.M., Guo, B.J., Li, Y.F., Yang, Z.Q., 2008. Tectonic implications from Re–Os dating of Mesozoic molybdenum deposits in East Qinling–Dabie orogenic belt. *Geochimica et Cosmochimica Acta* 72, 4607–4626.
- Mao, J.W., Xie, G.Q., Pirajno, F., Ye, H.S., Wang, Y.B., Li, Y.F., Xiang, J.F., Zhao, H.J., 2010. Late Jurassic–Early Cretaceous granitoid magmatism in Eastern Qinling, central-eastern China: SHRIMP zircon U–Pb ages and tectonic implications. *Australian Journal of Earth Science* 57, 51–78.
- Mao, J.W., Pirajno, F., Xiang, J.F., Gao, J.J., Ye, H.S., Li, Y.F., Guo, B.J., 2011. Mesozoic molybdenum deposits in the east Qinling–Dabie orogenic belt: characteristics and tectonic settings. *Ore Geology Reviews* 43, 264–293.
- Meng, X.J., Xu, W.Y., Lü, Q.T., Qü, W.J., Li, X.C., Shi, D.F., Wen, C.H., 2012. Zircon U–Pb dating of ore-bearing rocks and molybdenite Re–Os age in Shapinggou porphyry molybdenum deposit, Anhui Province. *Acta Geologica Sinica* 86, 486–494 (in Chinese with English abstract).
- Ni, Z.Y., Chen, Y.J., Li, N., Zhang, H., 2012. Pb–Sr–Nd isotope constraints on the fluid source of the Dahu Au–Mo deposit in Qinling Orogen, central China, and implication for Triassic tectonic setting. *Ore Geology Reviews* 46, 60–67.
- Padilla-Garza, R.A., Tittle, S.R., Eastoe, C.J., 2004. Hypogene evolution of the Escondida porphyry copper deposit, Chile. *Society of Economic Geologists Special Publication* 11, 141–165.
- Pearce, J.A., 1996. Sources and settings of granitic rocks. *Episodes* 19, 120–125.
- Perrelló, J., Sillitoe, R.H., Brockway, H., Posso, H., East, P., Solé, M., Stein, H., 2007. Chile: recent advances in the geology and evolution of a major Cu–Mo and Cu–Au porphyry system: ores and orogenesis. Abstracts of Symposium Honoring the Career of William R. Dickinson. Arizona Geological Society, Tucson, pp. 133–134.
- Peucat, J.J., Vidal, P., Bernard-Griffiths, J., Condie, K.C., 1988. Sr, Nd and Pb isotopic systematics in the Archean low- to high-grade transition zone of southern India: syn accretion vs. post-accretion granites. *Journal of Geology* 97, 537–550.
- Pirajno, F., 2009. *Hydrothermal Processes and Mineral Systems*. Springer, Berlin, (1250 pp.).
- Pirajno, F., 2013. *The Geology and Tectonic Settings of China's Mineral Deposits*. Springer, Berlin, (679 pp.).
- Richards, J.P., 2003. Tectono-magmatic precursors for porphyry Cu–(Mo–Au) deposit formation. *Economic Geology* 98, 1515–1533.
- Richards, J.P., 2009. Postsubduction porphyry Cu–Au and epithermal Au deposits: products of remelting of subduction-modified lithosphere. *Geology* 37, 247–250.
- Richards, J.P., 2011. High Sr/Y arc magmas and porphyry Cu ± Mo ± Au deposits: just add water. *Economic Geology* 106, 1075–1081.

- Richards, J.P., Chappell, B.W., McCulloch, M.T., 1990. Intraplate-type magmatism in a continent–island–arc collision zone: Porgera intrusive complex, Papua New Guinea. *Geology* 18, 958–961.
- Seedorff, E., Einaudi, M., 2004a. Henderson porphyry molybdenum system, Colorado: I. Sequence and abundance of hydrothermal mineral assemblages, flow paths of evolving fluids, and evolutionary style. *Economic Geology* 99, 3–37.
- Seedorff, E., Einaudi, M., 2004b. Henderson porphyry molybdenum system, Colorado: II. Decoupling of introduction and deposition of metals during geochemical evolution of hydrothermal fluids. *Economic Geology* 99, 39–72.
- Selby, D., Nesbitt, B.E., Muehlenbachs, K., Prochaska, W., 2000. Hydrothermal alteration and fluid chemistry of the Endako porphyry molybdenum deposit, British Columbia. *Economic Geology* 95, 183–202.
- Sillitoe, R.H., 1972. A plate tectonic model for the origin of porphyry copper deposits. *Economic Geology* 67, 184–197.
- Sláma, J., Košler, J., Condon, D.J., Crowley, J.L., Gerdes, A., Hanchar, J.M., Horstwood, M.S.A., Morris, G.A., Nasdala, L., Norberg, N., Schaltegger, U., Schoene, B., Tubrett, M.N., Whitehouse, M.J., 2008. Plešovice zircon—a new natural reference material for U–Pb and Hf isotopic microanalysis. *Chemical Geology* 249, 1–35.
- Smoliar, M., Walker, R., Morgan, J., 1996. Re–Os of group IIA, IIIA, IVA and IVB iron meteorites. *Science* 271, 1099–1102.
- Stacey, J.S., Kramers, J.D., 1975. Approximation of terrestrial lead isotope evolution by a two-stage model. *Earth and Planetary Science Letters* 26, 207–221.
- Steiger, R.H., Jäger, E., 1977. Subcommittee on geochronology: convention of the use of decay constants in geo- and cosmochronology. *Earth and Planetary Science Letters* 36, 359–362.
- Sun, S.S., McDonough, W.F., 1989. Chemical and isotopic systematics of oceanic basalts: implication for the mantle composition and process. In: Saunderson, A.D., Norry, M.J. (Eds.), *Magmatism in the Ocean Basins*. Geological Society of London Special Publication, 42, pp. 313–345.
- Sun, Y.L., Xu, P., Li, J., He, K., Chu, Z.Y., Wang, C.Y., 2010. A practical method for determination of molybdenite Re–Os age by inductively coupled plasma-mass spectrometry combined with Carius tube–HNO₃ digestion. *Analytical Methods* 2, 575–581.
- Tu, X.L., Hong, Z., Deng, W.F., Ling, M.X., Liang, H.Y., Liu, Y., Sun, W.D., 2011. Application of resolution laser ablation ICPMS in trace element analyses. *Geochimica* 40, 83–98 (in Chinese with English abstract).
- Waight, T., Baker, J., Peate, D., 2002. Sr isotope ratio measurements by double-focusing MC-ICPMS: techniques, observations and pitfalls. *International Journal of Mass Spectrometry* 221, 229–244.
- Wallace, S.R., 1995. SEG presidential address: the climax-type molybdenite deposits: what they are, where they are, and why they are. *Economic Geology* 90, 1359–1380.
- Wang, P., Chen, Y.J., Fu, B., Yang, Y.F., Mi, M., Li, Z.L., 2014. Fluid inclusion and H–O isotope geochemistry of the Yaochong porphyry Mo deposit in Dabie Shan, China: a case study of porphyry systems in continental collision orogens. *International Journal of Earth Science* 103, 777–797.
- Wei, Q.G., Gao, X.Y., Zhao, T.P., Chen, W., Yang, Y.H., 2010. Petrogenesis of Tangjiaping granite porphyry in northern Dabie: evidence from Zircon LA-ICPMS U–Pb dating and geochemical characteristics. *Acta Petrologica Sinica* 26, 1550–1562 (in Chinese with English abstract).
- Wiedenbeck, M., Alle, P., Corfu, F., Griffin, W.L., Meier, M., Oberli, F., Vonquadt, A., Roddick, J.C., Spiegel, W., 1995. Three natural zircon standards for U–Th–Pb, Lu–Hf, trace element and REE analyses. *Geostandard Newsletter* 19, 1–23.
- Wu, Y.S., Xiang, N., Tang, H.S., Zhou, K.F., Yang, Y.F., 2013. Molybdenite Re–Os isotope age of the Donggebi Mo deposit and the Indosinian metallogenic event in Eastern Tianshan. *Acta Petrologica Sinica* 29, 121–130 (in Chinese with English abstract).
- Xia, Q.X., Zheng, Y.F., Zhou, L.G., 2008. Dehydration and melting during continental collision: constraints from element and isotope geochemistry of low-T/UHP granitic gneiss in the Dabie orogeny. *Chemical Geology* 247, 36–65.
- Xiang, N., Yang, Y.F., Wu, Y.S., Zhou, K.F., 2013. Fluid inclusion study of the Baishan porphyry Mo deposit in the Eastern Tianshan ore field, Xinjiang Province. *Acta Petrologica Sinica* 29, 146–158 (in Chinese with English abstract).
- Xu, X.S., Griffin, W.L., Ma, X., O'Reilly, S.Y., He, Z.Y., Zhang, C.L., 2009. The Taihua group on the southern margin of the North China Craton: further insights from U–Pb ages and Hf isotope compositions of zircons. *Mineralogy and Petrology* 97, 43–59.
- Xu, X.C., Lou, J.W., Xie, Q.Q., Xiao, Q.X., Liang, J.F., Lu, S.M., 2011. Geochronology and tectonic setting of Pb–Zn–Mo deposits and related igneous rocks in the Yinshan region, Jinzhai, Anhui province, China. *Ore Geology Reviews* 43, 132–141.
- Xu, H.J., Ma, C.Q., Song, Y.R., Zhang, J.F., Ye, K., 2012. Early Cretaceous intermediate-mafic dykes in the Dabie orogeny, eastern China: petrogenesis and implications for crust–mantle interaction. *Lithos* 154, 83–99.
- Yang, Y.F., Li, N., Ni, Z.Y., 2009. Fluid inclusion study of the Jinduicheng porphyry Mo deposit, Hua County, Shaanxi Province. *Acta Petrologica Sinica* 25, 2983–2994 (in Chinese with English abstract).
- Yang, M.Z., Zeng, J.N., Qin, Y.J., Li, F.L., Wan, S.Q., 2010a. LA-ICP-MS Zircon U–Pb and molybdenite Re–Os dating for Qian'echong porphyry-type Mo deposit in Northern Dabie, China, and its geological significance. *Geological Science and Technology Information* 29, 35–45 (in Chinese with English abstract).
- Yang, Y.H., Wu, F.Y., Xie, L.W., Zhang, Y.B., 2010b. High-precision measurements of the ¹⁴³Nd/¹⁴⁴Nd isotope ratio in certified reference materials without Nd and Sm separation by multiple collector inductively coupled plasma mass spectrometry. *Analytical Letters* 43, 142–150.
- Yang, Y.F., Li, N., Wang, L.J., 2011. Fluid inclusion study of the Donggou porphyry Mo deposit, Henan province. *Acta Petrologica Sinica* 27, 1453–1466 (in Chinese with English abstract).
- Yang, Y.F., Li, N., Chen, Y.J., 2012. Fluid inclusion study of the Nannihu giant porphyry Mo–W deposit, Henan Province, China: implications for the nature of porphyry ore–fluid systems formed in continental collision regime. *Ore Geology Reviews* 46, 83–94.
- Yang, Y., Chen, Y.J., Zhang, J., Zhang, C., 2013a. Ore geology, fluid inclusions and four-stage hydrothermal mineralization of the Shangfanggou giant Mo–Fe deposit in Eastern Qinling, central China. *Ore Geology Reviews* 55, 146–161.
- Yang, Y.F., Chen, Y.J., Li, N., Mi, M., Xu, Y.L., Li, F.L., Wan, S.Q., 2013b. Fluid inclusion and isotope geochemistry of the Qian'echong giant porphyry Mo deposit, Dabie Shan, China: a case of NaCl-poor, CO₂-rich fluid systems. *Journal of Geochemical Exploration* 124, 1–13.
- Yuan, X.C., Klemperer, S.L., Teng, W.B., Liu, L.X., Chetwin, E., 2003. Crustal structure and exhumation of the Dabie Shan ultrahigh-pressure orogen, eastern China, from seismic reflection profiling. *Geology* 31, 435–438.
- Zartman, R.E., Doe, B.R., 1981. Plumbotectonics—the model. *Tectonophysics* 75, 135–162.
- Zhang, L.G., 1995. *Geology of East Asian Lithospheric-Isotope Geochemistry and Dynamics of the Upper Mantle, Basement, and Granitic Rocks*. Science Publishing House, Beijing, (252 pp.; (in Chinese with English abstract)).
- Zhang, Z.Q., Liu, D.Y., Fu, G.M., 1994. *Isotopic Geochronology of Metamorphic Strata in North Qinling*. Geological Publishing House, Beijing, (191 pp.; (in Chinese)).
- Zhang, H.F., Gao, S., Zhong, Z.Q., Zhang, B.R., Zhang, L., Hu, S.H., 2002. Geochemical and Sr–Nd–Pb isotopic compositions of Cretaceous granitoids: constraints on tectonic framework and crustal structure of the Dabieshan ultrahigh-pressure metamorphic belt, China. *Chemical Geology* 186, 281–299.
- Zhang, H.F., Sun, M., Zhou, M.F., Fan, W.M., Zhou, X.H., Zhai, M.G., 2004. Highly heterogeneous Late Mesozoic lithospheric mantle beneath the North China Craton: evidence from Sr–Nd–Pb isotopic systematics of mafic igneous rocks. *Geological Magazine* 141, 55–62.
- Zhang, H., Sun, W.D., Yang, X.Y., Liang, H.Y., Wang, B.H., Wang, R.L., Wang, Y.X., 2011a. Geochronology and metallogenesis of the Shapinggou giant porphyry molybdenum deposit in the Dabie orogenic belt. *Acta Geologica Sinica* 85, 2039–2057 (in Chinese with English abstract).
- Zhang, J., Chen, Y.J., Yang, Y., Deng, J., 2011b. Lead isotope systematics of the Weishancheng Au–Ag belt, Tongbai Mountains, central China: implications for ore genesis. *International Geology Review* 53, 656–676.
- Zhao, Z.F., Zheng, Y.F., Wei, C.S., Chen, F.K., Liu, X.M., Wu, F.Y., 2008. Zircon U–Pb ages, Hf and O isotopes constrain the crustal architecture of the ultrahigh-pressure Dabie orogeny in China. *Chemical Geology* 253, 222–242.
- Zhao, Z.F., Zheng, Y.F., Wei, C.S., Wu, F.Y., 2011. Origin of postcollisional magmatic rocks in the Dabie orogeny: implications for crust–mantle interaction and crustal architecture. *Lithos* 126, 99–114.
- Zheng, Y.F., Zhao, Z.F., Wu, Y.B., Zhang, S.B., Liu, X.M., Wu, F.Y., 2006. Zircon U–Pb age, Hf and O isotope constraints on protolith origin of ultrahigh-pressure eclogite and gneiss in the Dabie orogen. *Chemical Geology* 231, 135–158.
- Zheng, Y.F., Xiao, W.J., Zhao, G.C., 2013. Introduction to tectonics of China. *Gondwana Research* 23, 1189–1206.
- Zhu, R.X., Yang, Z.Y., Wu, H.N., Ma, X.H., Huang, B.C., Meng, Z.F., Fang, D.J., 1998. Palaeomagnetic constraints on the tectonic history of the major blocks of China during the Phanerozoic. *Science in China Series D* 41 (Suppl.), 1–19.